Catalytic and electrocatalytic performance of $Sr(Ti_{0.3}Fe_{0.7}Ru_{0.07})O_{3-\delta}$ for applications in Solid Oxide Fuel Cells supplied with ethanol steam reforming mixtures

Alessandro Donazzi[a,b*], *Travis A. Schmauss*[b], *Scott A. Barnett*[b*]

[a] Dipartimento di Energia, Politecnico di Milano, Via Lambruschini 4, 20156 Milano, Italy

[b] Department of Materials Science and Engineering, Northwestern University, Evanston (IL), 60208 USA

*corresponding authors:

Alessandro Donazzi, e-mail: alessandro.donazzi@polimi.it

Scott A. Barnett, e-mail: s-barnett@northwestern.edu

Abstract

Direct utilization of alcohols in Solid Oxide Fuel Cells (SOFCs) can improve the conversion efficiency by using excess heat for internal reforming and simplify the system balance of plant. Thanks to their scarce carbon-formation tendency, perovskite oxide anodes are promising alternatives to Ni-based cermets. Here we show that $Sr(Ti_{0.3}Fe_{0.7}Ru_{0.07})O_{3-\delta}$ (STF-Ru) exsolution anodes provide both catalytic reforming activity and electrochemical activity with steam/ethanol (S/E) mixtures at 3:1 and 2:1 molar ratio between 700 and 800°C. Electrolyte-supported scandia stabilized zirconia SOFCs with STF-Ru anodes and $Sr_{0.95}Ti_{0.3}Fe_{0.7}O_{3-\delta}$ (STF) cathodes are reasonably stable in the 3:1 S/E mixture over 20 h at 800°C, with maximum power density of 195 mW/cm^2 and 140 mW/cm^2 at 0.7 V. Deactivation instead occurs with the 2:1 S/E mixture. Comparatively, cells with Ni-YSZ anodes rapidly coke and fail under the same conditions. Ethanol steam reforming experiments in a fixed bed powder reactor reveal that, above 650°C, gas phase reactions convert ethanol to CO, hydrogen, acetaldehyde and ethylene, while STF-Ru catalyzes steam reforming. Thermogravimetric and Raman characterizations show that a moderate amount of carbon is deposited on the STF-Ru surface, which is more amorphous than the disruptive carbon which degrades Ni-YSZ.

Keywords: SOFC, exsolution, ethanol, Strontium titanate, carbon tolerance

1. Introduction

The worldwide commitment to deploy the access to cleaner electricity prompts the replacement of fossil fuels with renewable alternatives, and the use of more efficient power production methods with limited impact on the environment. In the United States and Europe, energy security targets require the reduction on oil dependency to be strictly accompanied by a significant mitigation of CO_2 emissions. Major efforts are hence put in decarbonizing the electricity production sector and the transportation sector, together responsible for ~50% of the global CO_2 emissions [1,2]. Currently, ethanol is the most promising non-petroleum renewable fuel, produced abundantly via fermentation of crops or sugarcane [3,4]. Taking advantage of biological CO_2 fixation, the use of ethanol as a fuel can lead to negative CO_2 processes if the emitted CO_2 were permanently captured and stored, a concept known as bioenergy with CCS (BECCS) [5].

Thanks to their high efficiency and unparalleled fuel flexibility, solid oxide fuel cells (SOFCs) can play a prominent role in decarbonizing both stationary and mobile applications. Thanks to the capability of transferring oxide ions across the electrolyte, SOFCs can process a variety of carbon-based fuels, including ethanol and other alcohols. In the transportation sector, ethanol fueled SOFCs can be used as range extenders in conjunction with batteries for light-duty vehicles, solving the shortcomings of slow start-up and shut-down of the stack [6,7]. Promising applications for SOFCs are also found in difficult-to-decarbonize transportation, such as long-distance transport and shipping of goods, wherein still a vast majority of the existing fleet neither relies on blends with high ethanol content (e.g. E85) nor on biofuels in general. A novel concept based on an onboard carbon capture and storage system has been recently proposed for commercial ships and long-range freight vehicles, the carbon capture fuel cell vehicle (CCFCV) [8]. In this concept, the SOFC is essential for power generation, since it produces non-diluted combustion exhaust (CO_2 and H_2O), which can then be further reduced to CO_2 alone by condensation of the water and stored. The direct supply of ethanol to the stack, via internal reforming rather than external reforming, improves fuel economy and reduces the tank volumes. In the first case, the SOFC directly supplies heat and steam to the reforming catalyst, with no need for burning part of the fuel to provide heat to a separate reforming unit, nor for integrating a heat exchanger.

The direct supply of ethanol to the SOFC anode is typically realized by exploiting the catalytic properties either of the anodic material itself or of a different material, which is coated on the top of the electrochemically active anode. In general, materials other than Ni-YSZ cermets are required to avoid deactivation, due to Nickel's extreme ability to catalyze carbon formation. Only a few authors [9,10] report feasible operations with Ni-YSZ cermets when supplying ethanol/steam mixtures with

a steam to ethanol (S/E) ratio larger than 3:1 on molar basis. Notably, from a stoichiometric viewpoint, this ratio is preferential to reform ethanol to H_2 and CO_2, while the 2:1 ratio produces a mixture of H_2 and CO. Too little steam leads to carbon deposition in the inlet part of the anode structure, worsening over time, and causing loss of electrochemical performance. Instead, excessively large amounts of steam in the feed mixture lead to a severe drop in the SOFC's efficiency, decreasing Nernst potential and net system efficiency if power is used to heat water. In contrast, coating the top of Ni-YSZ cermets with an appropriate catalytic layer allows the supply of even dry ethanol [11,12]. The concept of gradual internal reforming relies on the presence of a steam reforming catalyst, made of a noble or transition metal supported on doped cerium oxide (Gd-doped GDC or Sm-doped SDC), which allows the conversion of ethanol to syngas prior to its diffusion in the Ni-YSZ structure, avoiding coke deposition [13]. When dry ethanol is fed, the current extracted from the SOFC must be always high enough to produce sufficient steam for reforming. Ir/GDC layers [14,15] and core-shell Ni-Fe/GDC layers [11] are proved to be efficient, thanks to the fact that GDC provides effective ion transport, which allows the surface to be kept free of carbon deposits. A similar concept is also realized with metal supported SOFCs, wherein both the thick stainless steel support and the underlying anode are infiltrated with catalytically active elements, so that ethanol reforming is achieved before contacting the electrochemically active zone [16,17].

The replacement of Ni-YSZ allows to avoid an additional catalytic layer for reforming. In this case, the substituent anodic material must possess both catalytic and electrocatalytic activity to simultaneously reform and electro-oxidize ethanol, keep a C-free surface, and transfer electrons and ions. Several options are proposed in the literature [18–20]. Successful operation is reported with proton-conductive Ni-BZCY ($BaZr_{0.4}Ce_{0.4}Y_{0.2}O_{3-\delta}$ in [21], $BaZr_{0.4}Ce_{0.48}Yb_{0.1}Co_{0.02}O_{3-\delta}$ [22]), thanks to the enhancement of water adsorption, which benefits the gasification of carbon residues. GDC and SDC are also common choices for replacing YSZ in the anode cermet, given their high ionic conductivity, and their oxygen storage capacitance [19,23]. Nonetheless, the association of GDC and SDC with metallic Ni still leads to limited durability [6,20]. To solve this issue, Ni is either alloyed with or completely substituted by noble or transition metals. Thanks to its negligible tendency to form coke, Cu is preferential. However, its sluggish kinetic behavior requires the presence of a companion element, mostly Ce, Co and Ru, to enhance the electrocatalytic activity [24]. In order to boost the electrocatalytic and catalytic rates, these multi-metallic formulations are often prepared by infiltration of precursors solutions or by atomic layer deposition, which allow to reduce the particle size and enhance the extension of the contact surface between the active metal and the support [25,26].

Considering the importance of the metal particles size and of the oxygen transport properties of the support, exsolution of perovskites is a most promising technique to prepare ethanol tolerant

anodes. Thanks to their mixed ionic and electronic conductive (MIEC) properties, perovskites are excellent alternatives to cermets. However, even if the ionic conductivity limits the deposition of coke, the catalytic activity of perovskites in ethanol reforming is not comparable to that of supported transition or noble metals [23]. In exsolution systems, a metal cation is first incorporated into the lattice of a perovskite oxide, which acts as a host. Then, upon reduction, the metal emerges from the host perovskite, forming stable nanometric clusters on its surface which act as catalytic centers [27–29]. To date, only a few examples in the literature are dedicated to the utilization of exsolved perovskite anodes with ethanol. Sun et al. [30] show that electrolyte-supported LSGM cells with $SrBiFeTiO_{6-\delta}$ anodes achieve 30 h stable operations in dry ethanol at 800°C, with a power density of 100 mW/cm^2 at 0.7 V. Wan et al. [31] choose nickel vanadium strontium molybdate to exsolve Ni nanoparticles and show that electrolyte-supported LSGM cells also reach 100 mW/cm^2 at 800°C and 0.7 V with dry ethanol. The use of $La_{0.75}Sr_{0.25}Cr_{0.5}Mn_{0.5}O_{3-\delta}$ (LSCM) alone with ethanol is not successful [32,33]. Accordingly, Monteiro et al. [34] adopt LSCM-Ru anodes to achieve the exsolution of Ru nanoparticles and improve the performance of LSCM. Tolerance to carbon is observed, however, the power density is low, 80 mW/cm^2 at 950°C with dry ethanol.

In this work, the catalytic and electrocatalytic properties of $Sr(Ti_{0.3}Fe_{0.7}Ru_{0.07})O_{3-\delta}$ (STF-Ru) exsolution anodes are investigated in ethanol/steam mixtures. The electrochemical performance of STF-Ru is studied in electrolyte-supported scandia stabilized zirconia (ScSZ) cells operated between 700°C and 800°C with ethanol/steam mixtures at 3:1 and 2:1 S/E ratio, and compared with operation in humidified hydrogen. The resistance to coke formation and the catalytic performance of STF-Ru in the reaction of ethanol steam reforming is studied with experiments in a packed bed reactor. The homogenous reaction of ethanol steam reforming is also carried out in blank reactor tests, in order to understand its contributions and consequences. The catalytic and cell characteristics are compared with that for Ni-YSZ, tested under analogous conditions. Carbon deposits are analyzed with thermogravimetric and Raman experiments and the differences between Ni-YSZ and STF-Ru are rationalized. A promising performance emerges for STF-Ru upon exposure to 3:1 S/E mixtures.

2. Experimental

2.1 Materials synthesis and characterization

$Sr_{0.95}Ti_{0.3}Fe_{0.7}O_{3-\delta}$ (STF) and STF-Ru powders were synthesized via solid state reaction (SSR). In the case of STF, precursor powders of $SrCO_3$, TiO_4 (Sigma Aldrich) and Fe_2O_3 (Alpha Aesar) were ball-milled in ethanol for 100 hours with zirconia spheres as milling medium (180 g

spheres with 0.5 cm diameter plus 60 g spheres with 1 cm diameter for 20 g of precursors). The resulting suspension was dried at 60°C overnight, and then calcined at 1100°C for 10 h (5°C/min heating/cooling rate). In order to achieve an adequate particle size distribution, the calcined powders were ball-milled for additional 48 h prior to further use. In the case of STF-Ru, due to the hazardous reactivity of RuO_2 (Alfa Aesar) with organic solvents and especially ethanol, the SSR synthesis was performed by using water as a solvent with addition of a few droplets (< 0.5% v/v) of Triton X-100 (Sigma Aldrich) as a surfactant agent. 50/50 w/w Ni-YSZ cermet powders were also prepared by mixing equal amounts of NiO (Alfa Aesar, 400 mesh) and YSZ (Tosoh TZ 8-YS) and by following the same procedure of the SSR synthesis of the STF-based samples. The prepared powders were used for catalytic experiments and for the fabrication of electrolyte supported cells.

XRD patterns were recorded on the STF-based samples to verify the formation of the perovskite structure after calcination, and the successful achievement of metal particle exsolution after reduction. The BET (Brunauer-Emmett-Teller) method with N_2 adsorption (Tristar Micromeritics) was applied to determine the surface area (SA) of each synthesized sample, and of α-Al_2O_3 and quartz powders used as thermal diluent in the catalytic experiments. All the samples showed reversible type II isotherms, typical of non-porous or macro-porous adsorbents (Fig. S1 in the Supplementary Information document). The morphologic features of the SOFCs were analyzed with scanning electron microscopy (SEM) using a Carl Zeiss EVO50VP instrument equipped with an energy dispersive spectrometer (EDS). After exposure to reaction conditions during the catalytic experiments, transmission electron microscopy (TEM) and thermogravimetric analyses (TG-DTA) were performed on powder samples to evaluate the nature and the amount of the carbon deposits. The TG-DTA analyses were carried out with a simultaneous TG-DTG Seiko 6300 instrument: 20 – 30 mg of powders were first dried at 110°C for 1 h and then heated in air to 900 °C at 10°C/min. The particle size distribution of the powder samples was determined with laser granulometry (Cilas 1180). Prior to the analyses, the samples (~20 mg) were exposed to ultrasonic stirring in isopropyl alcohol for 10 min, in order to break the agglomerates.

2.2 Catalytic activity experiments

To investigate the catalytic activity of the synthesized samples in ethanol steam reforming, dedicated experiments were performed by supplying 50 sccm vaporized H_2O/ethanol mixtures with 3:1 and 2:1 S/E ratio on molar basis. The molar composition of the 3:1 mixture was 19.5% ethanol, 58.5% steam and 22% nitrogen, while the composition of the 2:1 mixture was 26% ethanol, 52% steam and 22% nitrogen. In the experiments, liquid solutions of water and ethanol (100% proof) were

injected in a vaporizing chamber maintained at 140°C, via a syringe pump (KD Scientific). 2.7 ml/h were supplied for the 3:1 mixture (52% ethanol, 48% water v/v), and 3 ml/h for the 2:1 mixture (62% ethanol, 38% water v/v). In all cases, 10 sccm nitrogen was used as a carrier to deliver the vaporized S/E mixture to the reactor. The samples were tested in a fixed bed tubular quartz reactor (5 mm inner diameter), equipped with a K-type thermocouple, heated by an electric furnace, and operated at atmospheric pressure. The catalytic powders were diluted in 1:10 ratio with α-Al_2O_3 to avoid thermal gradients in the fixed bed. To rule out parasitic effects due to the residual acidity of alumina, the original α-Al_2O_3 powders (Alfa Aesar, 99.98% ACS) were additionally fired at 1200°C for 10 h prior to mixing with the catalytic samples. This firing step reduced the surface area of the α-Al_2O_3 to 3 m^2/g. Selected experiments were repeated by using quartz as a diluent (SA < 1 m^2/g) in order to verify that the alumina was catalytically inactive, and the results revealed reproducible within the experimental precision. A set of experiments was also repeated by increasing the dilution ratio of the alumina to 1:20 and also in this case no difference was experienced, ensuring that no significant thermal gradients established in the fixed bed. The fixed bed consisted of 110 mg of diluted powders, which led to a gas hourly space velocity (GHSV) of 2.7×10^5 $Nl/kg_{cat}/h$ (8.6×10^5 h^{-1}). Prior to the experiments, the samples were reduced for 4 h in 3% humidified hydrogen, at 800°C in the case of STF-Ru and at 600°C in the case of Ni-YSZ. After reduction, the particle size distribution of STF-Ru showed a main peak centered at 110 µm followed by a smaller shoulder at 250 µm. The distribution of the Ni-YSZ powders is broader, with a first peak located at 250 µm and a second peak at 130 µm (Fig. S2). The reduced samples were diluted with alumina by ball-milling in ethanol for 48 h and drying for 24 h at room temperature to avoid reoxidation. This ball-milling step decreased the average particles size, and made it consistent with the powders used for the SOFC electrodes. Depending on the sample and on the S/E ratio, the experiments were performed between 600°C and 750°C by maintaining a constant temperature for 7 h while monitoring the composition of the gas products. Heating and cooling ramps to the target temperature were carried out at 5°C/min with N_2 to preserve the state of the catalyst surface. To evaluate the impact of the gas phase reactivity, all the experiments were also performed in a blank quartz rector, filled with 110 mg of the α-Al_2O_3 used for dilution. Repetition of these experiments with quartz powders did not show any appreciable difference.

The composition of the gas mixtures was measured with a gas chromatograph (GC, Agilent 7890A) equipped with a thermal conductivity detector (TCD) and a flame ionization detector (FID). H_2, CO, CH_4 and N_2 were separated by a molecular sieve column and detected by the TCD. Ethanol, CO_2, ethylene, ethane, acetaldehyde, dimethyl ether, and vinyl acetate were separated by a Plot-Q column and detected by the FID. The FID mounted a catalytic methanation unit (Jetanizer), which

allowed the conversion of CO and CO_2 to methane and increase the detection sensitivity to sub-ppm traces. Helium was used as carrier gas for both columns, with temperatures higher than 160°C to prevent water condensation. Each GC analysis took 20 minutes to complete. N_2 was taken as the internal standard for the quantitative determination of the measured compositions. To process the measured spectra, the response factors of the carbon-based species and of hydrogen were carefully determined with customized gas calibration tanks. In all the experiments, the C balances closed to within ±10%. The amount of water was calculated by closing the H balance.

2.3 Cells fabrication and electrochemical characterization

Electrolyte supported button cells with STF-Ru or Ni-YSZ anodes and STF cathodes were prepared by screen printing. Scandia stabilized zirconia substrates (140 μm thickness, 2 cm diameter, Fuel Cell Materials, Hionic) with 3 μm samaria doped ceria barrier layers were used as the electrolyte (Fig. S3). The inks for the electrodes were prepared by mixing the synthesized powders with Heraeus V-737 binder in 1:1.2 weight ratio, and then processing this suspension in a three roller mill. Before the preparation of the inks, the synthesized powders were ball milled in ethanol for 48 h and then dried at room temperature. The inks were screen printed on the electrolyte (0.5 cm^2 electrode area), dried at 150°C for 30 min, and fired for 4 h in air to reach adhesion, at 1100°C in the case of STF and STF-Ru, and at 1400°C in the case of Ni-YSZ. It is worth noting that never during the preparation of STF-Ru was the temperature maintained at higher than 1100°C, due to the volatility of Ru oxides, which is reported to become significant at ~1200°C. SEM analyses revealed that the thickness of the electrodes was ~20 μm (Fig. S3). Silver grids (Heraeus Conductor Paste T23 GM) were screen printed on the electrode surface and dried at 150°C overnight to form the current collectors. For the electrochemical tests, the cells were sealed on the top of alumina tubes with DAD-87 silver conductive paste (Shanghai Research Institute of Synthetic Resins). The performance of the cells was evaluated in a dedicated set-up consisting of a vaporization furnace maintained at 170°C and connected in series with a second furnace, where the testing tube was located. Care was taken in heating the fuel injector and its manifold to prevent condensation and formation of cold spots. Also in this case, a syringe pump was used to feed the water/ethanol mixture to the vaporizer. The cells were tested at 700, 750 and 800°C with the two ethanol steam reforming mixtures at 3:1 and 2:1 S/E ratio, and at 750 and 800°C with 3% humidified hydrogen. The S/E mixtures were identical in terms of composition and flow rate to those adopted for the catalytic experiments, except for 10 sccm Ar instead of N_2 for the carrier gas in the vaporizer. The experiments with the S/E mixtures were performed by supplying 50 sccm flow rate to the anode, and 150 sccm air to the cathode. The

experiments with humidified hydrogen were performed with 35 sccm anodic flow rate, and maintaining the same air flow. In a standard test sequence, a pristine cell was heated at 1°C/min in Ar up to 800°C and subsequently exposed to 3% humidified hydrogen for 4 h to reduce the anodic material. After the reduction, the cell was tested in humidified hydrogen to evaluate the reference performance, and then the target S/E mixture was admitted. Polarization (I/V) and electrochemical impedance spectroscopy (EIS) experiments were performed to characterize the electrochemical behavior of the SOFCs. The I/V curves were measured between OCV and 0.4 V by decreasing the voltage at 5 mV/s. When testing the S/E mixtures, the voltage was decreased 50 mV stepwise and held constant for 3 min. The resulting current was averaged in the range of 2 min. The EIS experiments were performed at OCV between 0.1 Hz and 100 kHz, with 10 mV voltage amplitude.

3. Results

3.1 Chemical characterization

The XRD patterns obtained on the STF-Ru powders before and after reduction are displayed in Figure S4. In line with previous studies [35,36], the pristine powders show peaks typically associated with a perovskite structure and consistent with the pattern of $SrTi_{0.3}Fe_{0.7}O_3$ (* symbol). This feature indicates that Ru is fully incorporated in the lattice, as a consequence of 10 h calcination at 1100°C. After 4 h reduction at 800°C in 3% humidified H_2 (4.09×10^{-22} P O_2), one additional peak becomes visible in the pattern of the reduced sample (● symbol) at 44.50° that can be reasonably ascribed to a metallic Ru-containing alloy (Fig. S4B). An unknown phase, possibly an impurity, is associated to the peak at 42.50°. Prior results suggest the presence of Ru-Fe alloy nanoparticles and possibly some Fe-rich particles [35], although the latter are not seen in the present results and the composition of the former could not be determined from these XRD results. The composition of these particles is expected to evolve with reduction time and with the H_2/H_2O ratio (i.e. ultimately with pO_2) [37]. As by TEM analysis in [35], the size of the exsolved particles ranges between 5 and 20 nm. The exposure to hydrogen also leads to a shift of the main perovskite peaks to lower angles (increasing lattice parameters) and to their broadening, due to the loss of oxygen from the structure. An estimation of the peak broadening at half height (from ~0.46° at 46.48° on the pristine sample to ~0.3° at 46.14° on the reduced sample) suggests that a change in the perovskite crystallinity occurs. Furthermore, the appearance of a shoulder peak at 31.6° is consistent with the partial formation of a double layer perovskite, which is caused by an excessive oxygen loss due to the severity of the reducing conditions. As shown by the BET analyses, the exsolution causes a growth of the surface area of the powders, from 11 m^2/g on the pristine samples to 17 m^2/g on the reduced samples. Notably,

the inclusion of Ru in the calcined perovskite also induces a moderate increase of the surface area compared to the STF perovskite used for the cathode (7.5 m^2/g).

3.2 Gas phase reactivity

Even when large amounts of steam are present, gas phase reactions play a key role in establishing the consumption rate of ethanol at high temperature [38–40]. Their interplay with the heterogeneous surface processes governs the success of a catalyst, in terms of conversion, lifetime and selectivity to the products. In order to investigate the impact of gas phase chemistry, the steam reforming of ethanol was performed in a blank quartz reactor filled with α-Al_2O_3 powders, under the same conditions adopted in the electrochemical experiments (section 3.5). Figure 1 displays the blank reactor results obtained with mixtures at 2:1 and 3:1 S/E ratio, between 600°C and 800°C, with 22% nitrogen dilution and 50 sccm flow rate. In line with the results of Liberatori et al. [38], the conversion of ethanol (panel A) is not significantly affected by the variation of the S/E ratio: the differences between the two curves in fact fall within the experimental variability. The activation of gas phase reactions occurs above 600°C, and a relevant conversion of ethanol is measured first at 625°C. At 700°C, 50% ethanol conversion is achieved, which grows to 80-85% at 750°C and becomes complete at 800°C. A temperature of 600°C can then be considered a limit for purely heterogeneous chemistry to activate, above which radical species begin to interact with the electrocatalyst surface. With respect to SOFCs, this result indicates that YSZ-based cells, typically active above 700°C, operate under conditions where gas phase reactions are responsible for a half or more of the ethanol conversion, which in turn can occur wherever the temperature is sufficiently high, for instance in the interconnectors' channels, in the gas supply lines and in the fuel injection manifold. Additionally, no ethanol reaches the cell at 800°C, and therefore the role of the anode becomes that of handling only gas phase products. The conversion of steam is reported in Panel B. Negative values are observed in the whole temperature range, which indicates that steam is produced instead of consumed. Panels C to F show the molar fractions of the main detected products, namely H_2, CO, methane, acetaldehyde, ethylene, and ethane. Ppm traces of ethyl acetate, vinyl acetate and dimethyl ether were also detected, but are not reported. No CO_2 was ever found among the products in relevant quantities. H_2 always prevails, and almost equimolar amounts of CO and methane are formed. Panels E and F display the molar fractions of acetaldehyde, ethylene, and ethane, which are secondary products of the process. Acetaldehyde and ethylene, well-known carbon precursors, are the main subproducts. The production of acetaldehyde peaks at 675°C at S/E of 3:1 and at 700°C at 2:1. After this peak, the acetaldehyde fraction drops quickly, and ethylene becomes the main subproduct. Notably, a larger amount of

ethylene is found at 2:1 S/E ratio, which suggests that this ratio is more favorable for coke formation compared to 3:1. The visual inspection of the quartz reactor revealed heavy coke formation after exposure to the 2:1 ratio at 800°C, whereas coke residues were almost absent in the case of the 3:1 ratio. This result also suggests that the 3:1 ratio is preferential to extend the lifetime of a catalyst.

Overall, the results of Figure 1 indicate that ethanol decomposition via dehydrogenation (Eq. 1) is the dominant conversion route, strictly followed by ethanol dehydration (Eq. 2). The absence of CO_2 among the products suggests that Water Gas Shift is not active and that the Boudouard reaction is not a relevant route for carbon formation. Moreover, the conversion of steam suggests that steam reforming (Eq. 3) does not occur, and therefore that the gas phase chemistry only entails the cleavage of the ethanol molecules (which is also consistent with the scarce sensitivity to the S/E ratio).

$$CH_3CH_2OH \rightarrow C_2H_4O + H_2 \qquad (1)$$

$$CH_3CH_2OH \rightarrow C_2H_4 + H_2O \qquad (2)$$

$$CH_3CH_2OH + H_2O \leftrightarrow 4H_2 + 2CO \qquad (3)$$

According to the evolution of the products with temperature, the dehydrogenation of ethanol is the major H_2 production source, followed by acetaldehyde decomposition to produce CO and CH_4 (Eq. 4). The dehydration of ethanol is also responsible for the production of ethylene, which is then partially hydrogenated to ethane (Eq. 5). Ethylene cracking (Eq. 6) and ethylene polymerization are instead major routes of carbon formation.

$$C_2H_4O \rightarrow CO + CH_4 \qquad (4)$$

$$C_2H_4 + H_2 \rightarrow C_2H_6 \qquad (5)$$

$$C_2H_4 \rightarrow 2C + 2H_2 \qquad (6)$$

3.3 Catalytic experiments

The catalytic activity of STF-Ru powders in the reaction of ethanol steam reforming was investigated to verify the resistance to carbon formation and the capability of converting ethanol. The experiments were performed by exposing the exsolved powders (i.e., reduced for 4 h in 3% humidified hydrogen, at 800°C) to steam/ethanol mixtures with 3:1 and 2:1 S/E ratio for 6 h, while measuring the composition of the outlet gas with a GC (section 2.2). No carbon formation is expected at equilibrium at 3:1 S/E ratio above 200°C, and therefore these experiments were repeated at 600°C, 650°C and 700°C. Additional experiments were also performed at 675°C and 750°C. The formation

of carbon is instead predicted starting from 650°C with 2:1 S/E ratio; hence, in this case, the experiments were conducted only at 650°C and 700°C [41]. For comparison, Ni-YSZ powders were also exposed to same reaction conditions of the STF-Ru powders.

3.3.1 Steam reforming experiments on STF-Ru powders

Panel A of Figure 2 shows the temporal evolution of the ethanol conversion, measured on the STF-Ru powders with the 3:1 S/E mixture. The dashed lines report the conversion of ethanol due to the gas phase reaction, measured during the experiments with no catalyst in the blank reactor, and the thermodynamic equilibrium conversion, which is equal to 100% under all the explored conditions. At time zero and 700°C, the conversion reached by the catalyst (95%) is close to the equilibrium but does not match it. Quickly, however, the conversion drops to 60% and then keeps reasonably constant for the rest of the experiment. Importantly, if the conversion matches the gas phase level, this would indicate that the catalytic activity is entirely suppressed. Indeed, even a spent catalyst, deactivated to an almost inert condition, would apparently lead to a measurable conversion due to the unavoidable presence of the homogenous reactivity. Hence, the observation of an ethanol conversion is not *per se* an indication of resistance to deactivation, rather the offset between the catalytic conversion and the homogenous one proves that the catalyst tolerates the reaction conditions. A similar picture is found at 650°C and 600°C. The initial conversion drops to a fairly stable level, which is higher than the gas phase limit (taken as zero at 600°C). The loss of initial activity is likely due to the deposition of solid carbon on the surface of the catalyst, although additional morphological changes cannot be excluded. Importantly, on the one hand, the presence of a measurable catalytic activity suggests that the form of carbon which is deposited on the STF-Ru surface does not entirely cover the sites active for the reaction, i.e. the exsolved Ru particles. On the other hand, this result also suggests that a stable condition is reached wherein some carbon is partially accumulated on the support surface, which is constituted by the STF perovskite, but it does not progress to suppressing the activity, possibly due to the oxygen transport properties of STF. The results show that the 3:1 S/E ratio guarantees stable activity after a period of approximately 1 h of catalyst conditioning (i.e. the process required to bring the surface to its stable configuration). Additional tests performed at 700°C with the 3:1 S/E ratio mixture (Fig. S5) confirmed that the catalyst performance is stable over the course of other subsequent 7 hours.

When the S/E ratio is lowered to 2:1, the picture clearly changes (Fig. 2B). In fact, the STF-Ru catalyst never reaches a stable condition, and the conversion drops to the gas phase level at each temperature. Complete conversion is initially achieved, and at 700°C the catalyst even maintains a

complete ethanol conversion longer than with the 3:1 mixture (for 90 minutes). Considering that the gas phase decomposition of ethanol is independent of the steam amount, these observations suggest that a high S/E ratio has a depressing effect on the reforming kinetic rate. Simultaneously, the increase of the ethanol concentration from 19% to 26% might have also prompted the reaction rate, revealing a positive reaction order. Hence, it can be speculated that the deactivation experienced by the STF-Ru catalyst might be due to an initially high ethanol consumption rate, which is not compensated by an equally high carbon gasification rate by steam, leading to excessive carbon accumulation and ultimately to deactivation. It is anyway well known since the early investigations [23] on catalytic steam reforming with transition and noble metals that the 3:1 S/E ratio is the lowest limit that a catalyst tolerates, while the 2:1 ratio typically leads to severe deactivation even under conditions where thermodynamics disfavor the formation of solid carbon. In Figure 2B, the experiment performed on the STF perovskite is also reported, in order to verify to what extent the reforming activity depends on the exsolved Ru particles. The results confirm that STF does possess an individual catalytic activity, in line with the oxygen exchange properties and consistently with other perovskite-based catalysts studied in the literature [23]. Nonetheless, the conversion drops faster than in the presence of Ru, which is then responsible for a consistent part of the catalytic conversion.

Irrespectively of the S/E ratio, a similar distribution of the products is achieved in the two experiments, although different amounts of the main species are measured. Figure 3 displays the molar fractions of the products as a function of the temperature during the experiment at 3:1 S/E ratio once a steady activity is reached. The dashed lines represent the amount measured during the gas phase experiment as well as the thermodynamic limits (reported with an additional star symbol). Striking differences are noted with respect to the results obtained with the blank reactor. The fractions of H_2 and CO have grown, and CO_2 is now detected. CH_4 passes through a peak centered at 675°C and then decreases, almost reaching the equilibrium at 700°C. These results suggests that the STF-Ru catalyst boosts ethanol steam reforming, and prompts the activation of the WGS reaction (Eq. 7) and of methane steam reforming (Eq. 8). Non negligible amounts of acetaldehyde, ethylene and ethane are still observed. Noteworthy, other than being exclusively originated from the gas phase, acetaldehyde is also produced by a surface pathway, as demonstrated by its presence at 600°C, at which no homogeneous chemistry is active. Acetaldehyde is in fact a well-stablished primary intermediate of the catalytic dehydrogenation of ethanol [23,39,40,42]. In contrast, ethylene and ethane (not reported) are absent at 600°C, and close to the homogenous level at 650°C, meaning that their source is not catalytic. This is a clear indication that STF-Ru can coexist with coke precursors, without suffering from quick deactivation, likely thanks to carbon gasification. Overall, a picture emerges where STF-Ru is capable of withstanding the supply of ethanol without experiencing

deactivation, possibly due to the intrinsic C-tolerant properties of noble metals and to the synergistic role of STF in providing extra oxygen to keep the surface sufficiently clean. This observation also agrees with other literature works dedicated to ethanol steam reforming on metal-exsolved catalyst [43–45], which show that durability is significantly improved thanks to the oxygen transport properties of the supporting perovskite.

$$CO + H_2O \leftrightarrow H_2 + CO_2 \qquad (7)$$

$$CH_4 + H_2O \leftrightarrow 3H_2 + CO \qquad (8)$$

3.3.2 Steam reforming experiments on Ni-YSZ powders

Ni-YSZ powders were also exposed to ethanol steam reforming mixtures at 3:1 and 2:1 S/E ratio, under the same conditions chosen for the STF-Ru samples. The temporal evolution of the ethanol conversion with the 3:1 S/E mixture is shown in Figure 2C. As expected, fast deactivation is experienced by the Ni-YSZ catalyst regardless of the S/E ratio. The ethanol conversion is always above the gas phase limit, and even remains complete at 600°C, but the C balance never reaches 80%, which is a clear indication of severe coking. Correspondingly, the reactor's pressure (Fig. 2D) shows a quick rise and the experiment had to be interrupted due to excessive pressurization. The deposition of solid carbon clogs the fixed bed of powders and leads to the pressure build-up. A steady and larger pressure rise is observed at 600°C, in line with the higher kinetic tendency to form coke in the intermediate temperature range, where the competing gasification routes might not be as active as at higher temperatures. When the 2:1 mixture is supplied (Fig. S6), a drop in ethanol conversion and a pressure rise are also observed: at 675°C after 5 hours, the ethanol conversion suddenly drops and matches the gas phase limit, indicating that the catalytic activity is completely suppressed. The dramatically fast coking rates observed at 675°C and 700°C on Ni-YSZ are further highlighted by considering that thermodynamic calculations predict no carbon formation above 650°C with the 2:1 S/E mixture. Comparatively, the temporal evolution of the inlet pressure during the experiments with STF-Ru is also reported in Figure 2D, which shows that no pressure build-up is experienced, neither with the 3:1 mixture nor with the 2:1 mixture.

The deactivation process revealed by the experiments on Ni-YSZ is in line with the formation of a disruptive form of carbon deposits, such as filaments, which detach the Ni particle from the YSZ support, and with the decay progress typically reported in reaction engineering practice [46,47]. During the growth, however, the Ni particle on top of the filament is still catalytically active, and maintains a relevant ethanol conversion, lagging the onset of a perceivable loss in the performance.

Therefore, while conversion might not be an immediate indicator of a catastrophic deactivation phenomenon, pressure build up is, since the filaments grow larger and longer and a block of solid carbon ends up plugging the reactor. To overcome this issue, fluidized bed reactor configurations are used by some authors [48].

Differently from Ni-YSZ, coke deposition on STF-Ru does not have such severe consequences. No pressure build-up is experienced by STF-Ru, even when it is driven to deactivation by the 2:1 mixture, and the powders remain unchanged to the eye after prolonged exposure to reaction conditions (Fig. S7). Additionally, STF-Ru and Ni-YSZ achieve almost the same particle size after dilution and milling with α-Al_2O_3, which rules out any possible effect due to different packing in the fixed bed. These observations strongly suggest that a non-disruptive form of carbon accumulates on the surface of STF-Ru.

3.4 Characterization of the carbon deposits

Considering their strikingly different coke-formation behavior, the STF-Ru and the Ni-YSZ powders were characterized after the catalytic experiments by means of DTA-TG, Raman and TEM analyses. The TG analyses (Fig. 4) were performed on Ni-YSZ samples tested at 700°C, and on STF-Ru samples tested at 650, 700 and 750°C. The results clearly show that the exposure to the 2:1 S/E mixture leads to larger coke formation compared to the 3:1 mixture, in line with the outcome of the catalytic experiments. The difference is more significant in the case of STF-Ru (0.2 mg/g_{cat} at 2:1 S/E vs. 0.05 mg/g_{cat} at 3:1 S/E at 700°C, Fig. 4E) and mirrors the distinction between the condition of catalyst survival at 3:1 S/E, and deactivation at 2:1. On the contrary, almost similar carbon amounts are found on the Ni-YSZ powders (Fig. 4F, $\geq$ 0.4 mg/g_{cat}), with almost no dependence on the S/E ratio, likely due to deep deactivation of the catalyst. Notably, carbon deposition on the STF-Ru catalyst shows a maximum as a function of temperature. The rise in carbon amount observed passing from 650°C to 700°C suggests a prevailing kinetic promotion of the carbon deposition rates over the carbon removal rates via gasification. At 750°C, a very limited amount of residue is found (0.02 mg/g_{cat} at 3:1 S/E), consistent with a kinetic increase of the carbon gasification rate. The TG profiles can be regarded as fingerprints of the carbon deposits, of which its peaks can be associated to structures with different nature and location with respect to the metal sites [48,49]. As a practical rule, the higher the peak temperature for the combustion, the less amorphous and more organized the carbon structure is. A peak at low temperature can be associated to the presence of polymeric carbon, while a shift to higher temperatures indicates that the structure possesses a more graphitic character. Encapsulating coke typically burns below 450°C and is located in the proximity of the metal particle,

which in turn helps in burning the deposit. Filamentous carbon burns above 550°C, and is separated by a larger distance from the metallic site. Heavily graphitic structures are removed above 700°C, due to their high level of graphitization and to stronger bonding to the support. The results of Figure 4 (panels A to D) broadly follow this picture. On Ni-YSZ powders, where filamentous structures prevail and the carbon accumulation is massive, all the peaks are found in the high temperature range, at 740°C after exposure to the 2:1 mixture, and at 670°C and 534°C with the 3:1 mixture. This latter peak would indicate that a fraction of carbon is still present which has not evolved into a high organization level. The peaks observed on the STF-Ru powders are shifted to lower temperature compared to Ni-YSZ. This result indicates that a less organized and less resistant type of carbon is formed, which can be removed more easily and which is most likely close to the Ru nanoparticles. Still, some exceptions are found that suggest the formation of filaments, such as the profile at 700°C and 2:1 S/E ratio, with a peak at 600°C, and the profile at 750°C and 3:1 ratio, with a peak at 640°C. The TG profiles collected on the STF-Ru samples also show that the main peaks shift to higher temperature going from 650°C to 750°C, confirming that more amorphous and less harmful carbon forms at lower temperature. Post-test TG analyses were also performed on STF-Ru and Ni-YSZ anodes exposed to 3:1 S/E mixtures during the electrocatalytic experiments (Fig. S8). Due to the small sample volumes and the resulting weakness of the load change signals, the TG balance was connected to a mass spectrometer to detect any possible formation of CO_2. No CO_2 signal was ever found on STF-Ru, whereas a CO_2 peak was regularly observed on Ni-YSZ. This picture agrees with the results obtained on the powder samples, and also suggests that the absence of coking on the STF-Ru anodes could be due to the beneficial effect of oxide ion transport, which could have removed all residual carbon when current was extracted (460 mA/cm^2 at 800°C).

Additional insight into the study of the carbon deposition is provided by Raman and TEM analyses (Fig. 5). All the Raman spectra show analogous features, that is, clear disordered D and graphitic G peaks (1380 cm^{-1} and 1590 cm^{-1} respectively) and less pronounced peaks in the 2D overtone region, one centered at 2700 cm^{-1} and a second at 2950 cm^{-1} [50]. Differences are experienced in the absolute intensity of the spectra and in the relative ratio between the intensity of D and G peaks (Table 1), which confirm the picture given by the TG investigation. The spectra of the Ni-YSZ powders show almost identical intensity and almost the same D/G ratio, regardless of the S/E ratio, which is consistent with heavy coking and with the minor differences in the TG profiles. On the STF-Ru powders, instead, both the D/G ratio and the absolute intensity of the spectra decrease in the samples exposed to the 3:1 S/E mixture. Furthermore, the D/G ratio and the spectra intensity increase upon cooling from 750°C to 700°C. These indications suggest that spectra with lower intensity are measured when a smaller amount of carbon is produced, and that a larger amount of

steam reduces the number of defects of the carbon deposits. This might suggest that the larger amount of steam reacts preferably with the amorphous species, while the more structured and graphitic kinds of species remain anchored to the surface. The TEM pictures collected on Ni-YSZ (Fig. 5B) and STF-Ru samples (Fig. 5C) exposed to the 2:1 S/E mixture at 700°C confirm the presence of filaments, consistently with the high temperature features of the TG profiles, i.e. the peak observed at 598°C in Figure 4B and most likely the other peaks found at similar temperatures.

3.5 Electrochemical testing of STF-Ru anodes with ethanol and hydrogen

Electrolyte supported STF-Ru/SDC/ScSZ/SDC/STF cells were tested at 700, 750 and 800°C with the two ethanol steam reforming mixtures, and with 3% humidified hydrogen at 750 and 800°C. Figure 6 displays the I/V curves collected with the 3:1 S/E mixture (panel A) and the I/V curves collected with humidified hydrogen (panel B). Switching from humidified hydrogen to the 3:1 S/E mixture causes the OCV to drop from 1.03 V to 0.88 V. The OCV values are reported in Table 2 and compared to the Nernst voltage values calculated with the molar fractions of H_2 and H_2O taken from the gas phase experiments in one case, and from the catalytic experiments on the STF-Ru powders in the other (section 3.3). The comparison shows that the OCV is closer to the predictions associated to the gas phase composition, than to those based on the catalytic experiment. The reason for this result is the difference between the GHSV obtained in the fixed bed of powders and the GHSV obtained in the set-up for testing the SOFCs. Namely, the amount of STF-Ru screen printed on the anode is ~2.5 times smaller than the amount used in the catalytic tests, while the gas flow rate is the same. A higher GHSV is thus realized in the SOFC set-up, which leads to a shorter contact time of the gas on the electrocatalyst, and ultimately to less ethanol conversion. Hence, the OCV measurements indicate that the composition of the mixture that reacts on the anode is predominantly the consequence of the gas phase chemistry and that the purely catalytic activity is limited. Upon decreasing the temperature, the maximum power density extracted during the S/E experiments decreases from 195 mW/cm^2 at 800°C to 125 mW/cm^2 at 750°C and 55 mW/cm^2 at 700°C (Fig. 6A and Table 3). The power density values are very low below 700°C, as a consequence of the electrolyte-supported nature of the ScSZ cell and of the limited amount of H_2 produced in the gas phase (3% H_2 at 650°C, Fig. 1). Qualitatively, at 800°C the negative curvature of the I/V curve above 350 mA/cm^2 suggests the onset of diffusional limitations that are not observed at 750°C and 700°C. Correspondingly, hydrogen utilization factors larger than 20% are achieved in the experiments with ethanol, which can possibly lead to the occurrence of compositional gradients (Table 3). Notably, a visual inspection of the alumina tubes downstream of the SOFC revealed the presence of carbon deposits after the I/V experiments; no

carbon was observed when the cells are maintained at OCV. This observation suggests that the extraction of current primarily leads to the conversion of ethanol into coke precursor intermediates, such as acetaldehyde, ethylene and CO, rather than to complete combustion products (i.e. H_2O and CO_2). Comparatively, being richer in the amount of fuel (97% H_2 vs. 16.2% H_2 + 11% CO + 9.3% CH_4 at 800°C, and 10.6% H_2 + 7.9% CO + 7.8% CH_4 at 750°), the experiments with humidified H_2 show better performance (400 mW/cm^2 at 800°C and 250 mW/cm^2 at 750°C) and no evidence of a limiting current in the I/V curve. In this case, the cell operates with limited hydrogen utilization factors (≤ 11%) and almost differential regime.

The EIS experiments were performed at OCV. The results obtained with the humidified hydrogen mixture (panels A and B of Fig. 7) show two arcs, one located at high frequency between 10 kHz and 100 Hz, and a second larger arc in the low frequency region, between 100 Hz and 0.1 Hz. This is a typical shape for STF-Ru based cells in previous works [35,51]. The ohmic resistance R_{ohm} is 0.28 Ω cm^2 at 800°C and 0.39 Ω cm^2 at 750°C at OCV. As expected, the polarization resistance R_{pol} increases upon reducing the temperature due to slower kinetics, from 0.26 Ω cm^2 at 800°C to 0.55 Ω cm^2 at 750°C. The EIS experiments performed with ethanol supply (panels C to E of Fig. 7) show that that all the arcs have a high frequency branch with π/4 slope, followed by a second larger arc at low frequency. A similar shape, which also looks similar to a Warburg arc, is found at OCV by Cimenti et al. [32] when feeding a LSCM-based anode with pure ethanol, and is attributed to diffusive limitations due to plugging of the pores by carbon deposits. In the present case, however, considering that the anodes are only ~20 μm thick (Fig. S3), a significant diffusive limitation due to occlusion of the pores is unlikely. Instead, if the kinetic rates are not sufficiently high, the electrochemically active thickness becomes comparable or even equal to the anode thickness, and the impedance spectrum typically shows a large arc at low frequency.

3.6 Equivalent circuit analysis

The impedance spectra collected at OCV with humidified H_2 and with the 3:1 S/E mixture were quantitively analyzed with the equivalent circuit method. The best fit was achieved with the circuit reported in Figure S9, which includes the ohmic resistance of the ScSZ electrolyte, connected in series with three RC elements and one RQ element. These elements are represented in order of decreasing characteristic frequency, meaning that the frequency of RC_1 is higher than the frequency of RC_2 and so on. Hence, RC_4 has the lowest frequency. The adequacy of the equivalent circuit was verified by application of the chi squared test χ^2, which resulted in a confidence level of 90% for the estimates of the parameters. An error bar also calculated for each parameter, based on this confidence

interval and on the standard deviation of the residual squared errors of the model simulations. Table S1 of the Supplementary Information document reports the values of the circuit elements fitted to the spectra. The results show that the resistance, the frequency and the capacitance of RC_1 and RC_2 keep almost constant when switching from humidified H_2 to the S/E mixture. Hence, these arcs can be associated to the STF cathode of the cell, which is not subject to kinetic variations due to a change in the anodic mixture. The frequency of RC_1 shifts from 1.3 kHz at 800°C to 0.9 kHz at 750°C, and further decreases to 0.7 kHz at 700°C. The frequency of RC_2 passes from 100 Hz to 65 Hz in the same temperature range. The RC_1 arc possibly represents the resistance of the processes taking place at the STF/SDC interface, while the RC_2 arc describes the surface processes at the STF/gas interface, which are typically found at lower frequency. Similar frequency ranges and resistance values are also reported by Zhang et al. [52] in a study dedicated to STF cathodes. The parameters of the other two arcs, RQ_3 and RC_4, change when passing from humidified H_2 to the S/E mixture. Accordingly, these arcs are associated to the kinetics of the STF-Ru anode. The frequency of RC_4 passes from 3 Hz to 1 Hz between 800°C and 700°C, and that of RC_4 shifts from 2 Hz to 0.6 Hz. Note that the frequency of all the circuit elements decreases upon decreasing the temperature, in agreement with the drop of the reaction rates and the consequent growth of characteristic time constants. Figure 7F displays the activation energy E_{act} of each resistance for the experiments with the S/E mixture. 75.5 kJ/mol are also calculated for E_{act} of R_{ohm} (which is the only parameter not fitted but directly taken from the measurements), in agreement with the expected activation energy for oxide ion transport in ScSZ. Small pressure variations in the ethanol injection and vaporization system, which occurred in the order of a few seconds, caused some scatter in the spectra below 1 Hz, and hence only a few well-reproducible impedance points were considered. In this low frequency branch, which is associated to the effect of R_4, a larger error bar is calculated (maximum 10.5%), which leads to larger uncertainty in the estimation of E_{act} (188 ±18 kJ/mol), while a more accurate fitting is obtained for all the other polarization resistances (49 ±2 kJ/mol for R_1, 69 ±4 kJ/mol for R_2 and 118 ±7 kJ/mol for R_3). Aside of the uncertainty range, the results confirm that none of these resistances is associated to gas diffusion effects, rather to kinetics, since gas diffusion is almost insensitive to temperature.

3.7 Deactivation behavior

In order to preliminary investigate the effects of exposing the cell to the 3:1 S/E mixture, I/V curves were periodically collected at 800°C, and the comparison is reported in Figure 8A. The reference I/V curve refers to the performance obtained after an initial conditioning period of 90 min, which is given to the cell to achieve a steady state OCV value. A limited loss of performance, which

barely affects the I/V behavior, is experienced by the cell after 2 h time on stream, if compared to the reference curve. After 20 h exposure to the 3:1 S/E mixture, the performance further decreases, and the final power density settles at 156 mW/cm^2. Correspondingly, the I/V curve flattens out and the shape becomes almost linear. The general trend is that the cell performance decreases with time and exposure to the S/E mixture. The analysis of the EIS spectrum collected at OCV after 20 h (Fig. 8B) reveals that R_{ohm} is subject to a substantial increase from 0.28 Ω cm^2 to 0.38 Ω cm^2 (+36%), whereas R_{pol} keeps constant at ~0.46 Ω cm^2, which suggests that the main reason for a loss of activity stems from the increase of a static resistance, possibly due to the deterioration of the silver contacts. As a matter of fact, previous works dedicated to STF-based electrodes [37,51] do not report a degradation of the electrode/electrolyte contact due to delamination or cracking, but still show a performance decay at the beginning of any set of experiments or life-test analysis. The experiments at 750°C and 700°C were performed between 2 and 8 h, then the cell was heated back to 800°C and kept at OCV. No appreciable decrease of the OCV was observed between 8 and 20 h with the 3:1 S/E mixture (Fig. 8C). This result agrees with the stable behavior observed in the 14 h durability experiments on the STF-Ru powders (Fig. S5).

The degradation behavior was also explored on the STF-Ru anodes with the 2:1 S/E mixture and on the Ni-YSZ cermet anodes with the two S/E mixtures. In line with the catalytic experiments, exposing the STF-Ru based cell to the 2:1 S/E mixture leads to quick deactivation. The results of Figure 8D show that the I/V performance measured at 750°C drops within a few hours. Starting from an initial power density of 155 mW/cm^2, after 4 h the I/V curve has a steep decay to 80 mW/cm^2, with the appearance of a limiting current below 0.3 V, possibly due to carbon deposits that clog the anode's pores. After 16 h, the OCV drops and the cell is completely deactivated. The experiments were repeated also with cells mounting Ni-YSZ anodes, identical to the cells tested with STF-Ru anodes. Under no condition the anode survives the exposure to the ethanol steam reforming mixture, at both 3:1 (Fig. 8E) and 2:1 S/E ratios (Fig. 8F). Simply keeping the cell at OCV leads to a slow decay and ends in an abrupt failure. These results can be rationalized on the basis of the behavior observed in the catalytic experiments, as well as by considering that thin anodes were used (~20 μm). On the one hand, the severe drop of the OCV is accompanied by the physical loss of the Ni-YSZ electrocatalyst. A visual inspection of the cell after the experiments in fact revealed complete delamination of the Ni-YSZ anode from the electrolyte. This was probably due to excess of coking and detachment between the Ni and YSZ particles. On the other hand, other authors [9,10] report that standard anode-supported Ni-YSZ cells (~1 mm) are able to withstand the supply of S/E mixtures at 3:1, although carbon deposits in the first microns of the anode, which is indeed comparable to the thickness of the current Ni-YSZ cermet. Other than a thicker anode, the extraction of current might

have also helped in keeping the deactivation rates lower, by removing the deposited carbon. Nonetheless, the present results might also suggest that much longer experiments are required to appreciate further progress of the carbon deposition front until reaching a full deactivation also on anode-supported cells, as experienced by other authors [19].

4. Discussion

Promising preliminary results are obtained by application of STF-Ru anodes in SOFCs supplied by ethanol steam reforming mixtures at 3:1 S/E ratio. STF-Ru limits the formation of carbon and tolerates the accumulation of deposits without deactivation over the course of at least 20 h. The slight performance loss observed during cell operation is normal for this type of electrodes, and the temperature programmed oxidation results (Fig. S8) show that no coking is present, suggesting that cell operation in ethanol could stabilize in the long term. Similar modifications with time on stream are also typically experienced with H_2, and cannot be specifically ascribed to ethanol. Comparatively, the use of a standard Ni-YSZ cermet shows a hyper production of carbon, which leads to dramatically rapid plugging of the fixed bed of catalytic powders (Fig. 2) and to mechanical failure of the anode during the electrochemical experiments. This comparison reveals interesting consequences: STF-Ru forms a relatively small amount of a *non-disruptive* type of carbon, while Ni-YSZ prompts the production of *disruptive* carbon. As suggested by the thermogravimetric profiles (Fig. 4), the type of carbon deposited on the STF-Ru surface is less structured and more amorphous than that found on Ni-YSZ, and ultimately proves less harmful. After exposure of the STF-Ru samples to the 3:1 S/E mixture, the main peaks due to coke combustion are found at low temperature (400 – 450°C), which suggests proximity to the metal sites and higher accessibility in the porous texture of the catalyst [49]. Secondary smaller peaks are observed between 520°C and 650°C, which correspond to filamentous carbon, and which also represent the sole deposit after the experiment at 750°C. Overall, the net amount of coke accumulated on STF-Ru is eight times less than on Ni-YSZ, and two to four times less than on STF-Ru samples exposed to the 2:1 S/E mixture. This favorable situation might be due to intrinsically slow rates of carbon formation on Ru nanoparticles, but also to the beneficial contribution of the STF perovskite, which allows to more efficiently oxidize the carbon deposits by supplying oxide ions. Depending on the stoichiometry of Sr in the perovskite, indeed, an oxide ion conductivity between 3×10^{-3} and 2×10^{-2} S/cm is found by Nenning et al. [53] at 650°C under reducing atmosphere (10^{-21} to 10^{-25} P O_2), while Jung and Tuller report up to 3×10^{-2} S/cm at 800°C in oxidizing conditions [54]. Hence, a favorable balance among gasification rate, carbon formation rate and carbon oxidation rate is established on STF-Ru, which instead is not realized on Ni-YSZ under the same

conditions. Even if YSZ is also capable of transferring oxide ions and therefore contribute to coke removal, since its conductivity is similar to STF (4.3×10^{-2} S/cm at 800°C and 1.16×10^{-2} S/cm at 650°C from [55]), the morphological features of the cermet are less favorable. One order of magnitude smaller SA is measured on the Ni-YSZ cermet (1 m^2/g) compared to the exsolved STF-Ru samples (17 m^2/g) and to the STF support (10 m^2/g), which significantly reduces the extension of the active contact area between Ni and YSZ and proves that the surface capable of supplying oxygen is lower. Hence, the contribution of the oxygen transport properties is smaller in the Ni-YSZ cermet, and the coke formation tendency of Ni is not counterbalanced. Early literature examples [9,10] wherein a stable performance by the Ni-YSZ anode in ethanol is claimed, do neither report lifetime testing, nor check for the presence of carbon residues.

The comparison between the morphologic properties of Ni-YSZ and STF-Ru suggests additional observations. Even if the surface area is smaller, the conversion of ethanol achieved with the Ni-YSZ cermet in the steam reforming experiments (70% at 700°C and 3:1 S/E, Fig. 2C) is higher than that achieved with STF-Ru (60% at 700°C and 3:1 S/E, Fig. 2A), at least in the first hours of reaction before collapsing, and the product distribution is closer to the equilibrium, with increased rates of H_2 production. Instead, when tested at the same GHSV, the steady state conversion of ethanol on STF-Ru always maintains moderately above the gas phase conversion, with a product distribution which still resembles the early stages of the reforming process until 675°C. Notwithstanding the effect of the increased pressure, on the one hand, the results of the catalytic experiments corroborate the extremely high activity of Ni in ethanol reforming, accompanied by an equally high C accumulation tendency, which can be moderated by doping support (e.g. with La, Ce or Mg) [46]. On the other hand, the experiments of ethanol steam reforming show that STF-Ru has sluggish kinetic rates, which however disfavor coke deposition and ultimately allow the catalyst to avoid deactivation. Other literature works support that Ru has sluggish kinetics compared to other noble metals and to Ni. The operative conditions adopted in this work are representative of up to one order of magnitude shorter contact times than typical (2.7×10^5 $Nl/kg_{cat}/h$ GHSV vs. 1.6×10^4 $Nl/kg_{cat}/h$ in [38], 4×10^4 $Nl/kg_{cat}/h$ in [56] and 5.5×10^3 – 3×10^5 h^{-1} in [57]) and are not optimal to promote the catalytic performance. Yet, very similar ethanol conversion and product distribution is achieved by Liguras et al. [40] who worked at 2×10^5 $Nl/kg_{cat}/h$ GHSV with 1% w/w $Ru/\gamma Al_2O_3$ catalysts: notably, these authors had to increase the amount of Ru from 1% to 5% w/w, in order to improve the catalytic activity and match the conversion of other noble metals tested at 1% w/w (Rh, Pt, Ir). Considering that the exsolution leads to alloyed Ru-Fe nanoparticles [35], it can be also speculated that Fe plays a role in the reforming kinetics and coke formation, as suggested by the literature [58]. O'Shea et al. [59] report a promotion of the ethanol reforming rates and a decrease of the selectivity to CH_4 and CO when

alloying Co with Fe; Domínguez et al. [60] find a favorable effect by doping Co-based silicates with Fe for applications in steam reforming experiments; alloying Ni with Fe is a preferential solution for supported catalysts used in the gasification and reforming of biomasses and tars [61].

The supply of ethanol steam reforming mixtures to SOFCs reveals several interesting features concerning the catalytic and electrocatalytic behavior of the anode. Due to the occurrence of gas phase reactions, a complex chemical environment is established at the anode of stabilized zirconia-based cells, which preferentially operate above 700°C. The results of the dedicated catalytic experiments (Fig. 3) show that 50% of the ethanol supplied is converted at 700°C by homogeneous reaction routes and that the amount of coke precursor products, such as acetaldehyde and ethylene, is comparable to the amount of H_2 and CO. At 800°C, complete ethanol conversion is achieved, but the mixture which reaches the anode of the cell is far from the thermodynamic equilibrium composition, and still contains acetaldehyde and ethylene. Similar results have been reported by several authors [38–40] with S/E ethanol mixtures at different steam content and dilution (from 50% N_2 dilution up to no dilution) consistently indicating that the conversion of ethanol and the distribution of the products are almost insensitive to the amount of steam. Experiments of gas phase oxidative steam reforming of ethanol [62] also reveal that the addition of O_2 suppresses the formation of acetaldehyde, but does not prevent the production of ethylene, which is a strong coke formation precursor via polymerization and cracking. The scarce sensitivity of gas phase chemistry to ethanol co-reactant, due to the primary activation of dehydrogenation and dehydration routes, also poses an issue concerning the direct supply of anhydrous ethanol. As a matter of fact, the SOFC does not operate with a fully reformed mixture, rather, it operates in a chemical environment highly susceptible of accumulating carbon also on the surface of the fuel supply tubing, and in all those parts that are heated up to the operative temperature of the cell. From a technological viewpoint, this is an issue with respect to the scale-up to applicative systems. In agreement with the literature [23,42], the present results show that 650°C is a reasonable threshold for the activation of gas phase chemistry. Below 650°C the ethanol conversion is exclusively catalytic, a result which suggests that low to intermediate temperature cells can suppress the issue of carbon accumulation in the manifold, but require a sufficiently active catalyst at the anode. Instead of substituting STF-Ru, the sluggish reforming kinetics can be compensated by making a relatively thick anode or reforming layer. A preliminary estimation of the thickness of this layer can be done by considering the results of the experiment performed on the STF-Ru powders at 600°C with 50 sccm 3:1 S/E mixture, which gave an ethanol conversion of ~15% (Fig. 2A). The complete calculations are reported in the Supplementary Information document. Assuming that the packed bed of powders can be treated as an isothermal plug flow reactor (40% void volume, 10 mg catalyst, 5.24 g/cm^3 STF-Ru density), and that the rate of ethanol steam reforming

is first order dependent on the concentration of ethanol ($r = k \cdot C_{EtOH}$), the rate of reaction can be estimated according to equation 9, where Q^0 represents the inlet volumetric flow rate, and V the reactor volume [63]. Based on 0.78 expansion coefficient ε_{SR} for the ethanol steam reforming reaction (19.5% ethanol inlet molar fraction), a rate constant k of 1.38×10^{-2} s^{-1} is found. Then, on further assuming that the SOFC anode behaves as an isothermal continuously stirred tank reactor (CSTR), the volume required to reach a target conversion can be calculated with equation 10. In turn, the thickness required by the electrode is derived, considering for instance 30% porosity. In order to explore a realistic case, this estimation can be done considering an anode-supported cell of applicative size which operates in a stack, for instance with 225 cm^2 area and supplied by 1 slpm of 3:1 S/E mixture at 600°C. Reasonably thin STF-Ru layers are calculated, namely 20 µm to achieve 50% ethanol conversion and 67.5 µm for 75% conversion. Noteworthy, these predictions represent the minimum possible layer thickness, since equilibrium limitations are not included (approaching the thermodynamic equilibrium slows the kinetic rates), mass transport limitations are neglected, the reaction mechanism involves additional steps than the sole steam reforming, and temperature gradients are certainly established when the conversion of ethanol increases. Even if these additional constraints would give rise to thicker layers, the preliminary estimation indicates that a STF-Ru anode would not require an exceedingly large thickness in real applications.

$$k\frac{V_{PFR}}{Q^0} = (1+\varepsilon_{SR})ln\frac{1}{1-\chi_{EtOH}} - \varepsilon_{SR}\chi_{EtOH} \quad (9)$$

$$k\frac{V_{CSTR}}{Q^0} = \frac{\chi_{EtOH}(1+\varepsilon_{SR}\chi_{EtOH})}{1-\chi_{EtOH}} \quad (10)$$

5. Conclusions

In this work, the performance of $Sr(Ti_{0.3}Fe_{0.7}Ru_{0.07})O_{3-\delta}$ perovskite oxide (STF-Ru) as anode for solid oxide fuel cells supplied with steam/ethanol mixtures is investigated between 700 and 800°C. Electrolyte supported ScSZ cells (140 µm) mounting STF cathodes are tested with mixtures at 3:1 and 2:1 S/E ratio and 22% inert dilution, with I/V and EIS measurements. The catalytic properties of STF-Ru powders are also studied in dedicated experiments, under the same conditions adopted for the SOFC testing. STF-Ru tolerates the supply of 3:1 S/E mixtures without major coke formation nor deactivation over the course of 14 hours. Deactivation occurs instead after exposure to 2:1 S/E mixtures. Below 750°C, amorphous carbon is primarily found with smaller amounts of filamentous carbon. Comparatively, analogous catalytic experiments carried out on Ni-YSZ powders reveal severe deactivation, with accumulation of up to ten times more carbon and quick plugging of the reactor. A positive synergy between Ru and STF occurs, which allows limited carbon accumulation

thanks to the oxide ion conductivity of STF, and leads to the formation of non disruptive deposits, clearly distinguished from the disruptive kind observed on Ni-YSZ. Considering the impact of gas phase reactions above 700°C, which form significant fractions of coke precursors (acetaldehyde and ethylene) and favor carbon monoxide over hydrogen, the main role of thin STF-Ru anodes is to provide a barrier against coking, more so than reforming the ethanol feed. Promising preliminary electrochemical performance is found on SOFCs with STF-Ru anodes in terms of power density (190 mW/cm^2 at 800°C) and durability. In the light of the present results, the following strategies are proposed to improve the performance of STF-based cells:

- The present cells with STF-Ru anodes can work at temperatures of ~800°C with direct ethanol internal reforming. The limited coking observed may cause problems in long-term operation, this could perhaps be reversed by periodically removing the coke with a redox cycle, which STF-Ru anodes are known to survive without degradation [35]. Even though the ethanol conversion in the present anodes was low, in larger area cells with somewhat thicker anodes, the conversion should be sufficient.
- Ni-STF exsolution anodes [37] might provide an interesting alternative to STF-Ru, taking advantage of the higher catalytic activity of Ni with the favorable properties of STF. In the form of nanoparticles, Ni is expected to be more active, and alloying with Fe should improve coke resistance.
- Lowering the operative temperature allows to significantly limit the impact of gas phase chemistry, and even suppress it below 600°C. In turn, this condition limits the production of coke precursors. Lower temperatures should benefit also the conditions of the SOFC supporting manifold, avoiding the deposition of coke in the fuel injector, in the interconnector channels and in all those parts which are heated up to high temperature without the presence of a catalyst. Note that thin-electrolyte cell designs will be required to achieve useful power densities at temperatures ≤ 650°C [51,64]. Although a reduced temperature decreases ethanol conversion, this can be compensated by increasing the thickness of the STF-Ru anode, increasing the conversion of ethanol and thereby improving the cell performance.

Acknowledgements

The authors gratefully acknowledge financial support by the Department of Energy Basic Energy Sciences, grant # DE-SC0016965. Alessandro Donazzi gratefully acknowledges the U.S.-Italy Fulbright Program for granting a research scholarship.

Tables

Table 1 – Average D/G intensity ratio as a function of temperature and S/E ratio for the Ni-YSZ and the STF-Ru powder samples.

Sample	D/G	S/E	T [°C]
Ni-YSZ	0.97	3.0	700
	0.95	2.0	700
STF-Ru	1.06	3.0	750
	1.14	2.0	750
	1.14	3.0	700
	1.31	2.0	700

Table 2 – Comparison between the OCV measured with the 3:1 S/E mixture and the Nernst voltage calculated for H_2 based on the composition of the gas phase chemistry experiments and of the catalytic experiments with STF-Ru. The thermodynamic equilibrium composition is assumed at 800°C for the catalytic experiments.

		Gas phase chemistry			Catalytic chemistry		
T [°C]	**OCV [V]**	**H_2**	**H_2O**	**E_N [V]**	**H_2**	**H_2O**	**E_N [V]**
800	0.877	0.162	0.439	0.889	*0.494*	*0.163*	0.987
750	0.883	0.106	0.506	0.882	0.465	0.165	0.997
700	0.885	0.053	0.566	0.857	0.246	0.391	0.948

Table 3 – Performance indicators of the STF-Ru based SOFCs during the experiments with humidified H_2 and the 3:1 S/E mixture. The utilization factors U_F are calculated on the basis of H_2. In the case of the 3:1 S/E mixture, the inlet molar fraction of H_2 is taken from the results of Figure 1.

T [°C]	H_2	Power Density [mW/cm^2]	U_F
800	97%	400	11.1%
750	97%	255	7.3%
800	16.2%	195	21.8%
750	10.6%	124	26.4%
700	3.6%	55	35.4%

Figures

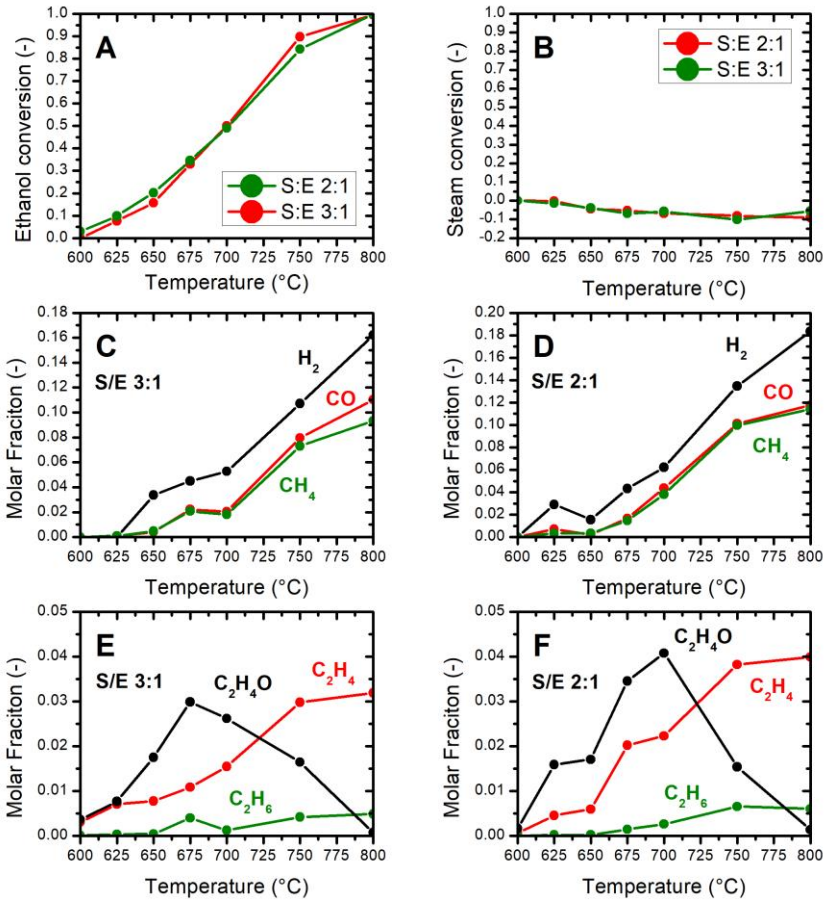

Figure 1

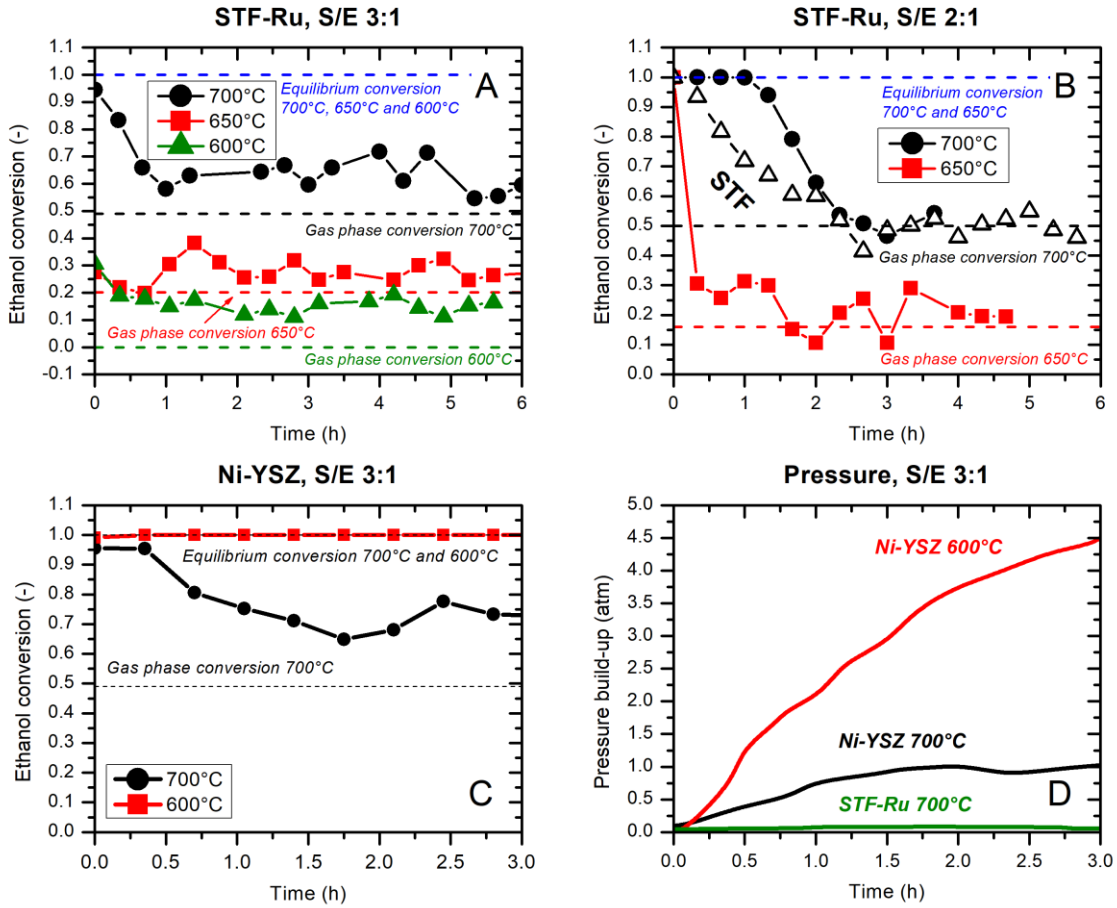
STF-Ru, S/E 3:1
Ethanol conversion (-)
Time (h)
700°C
650°C
600°C
Equilibrium conversion
700°C, 650°C and 600°C
A
Gas phase conversion 700°C
Gas phase conversion 650°C
Gas phase conversion 600°C
STF-Ru, S/E 2:1
Equilibrium conversion
700°C and 650°C
B
STF
Ni-YSZ, S/E 3:1
Equilibrium conversion 700°C and 600°C
C
Pressure, S/E 3:1
Pressure build-up (atm)
Ni-YSZ 600°C
Ni-YSZ 700°C
STF-Ru 700°C
D

Figure 2

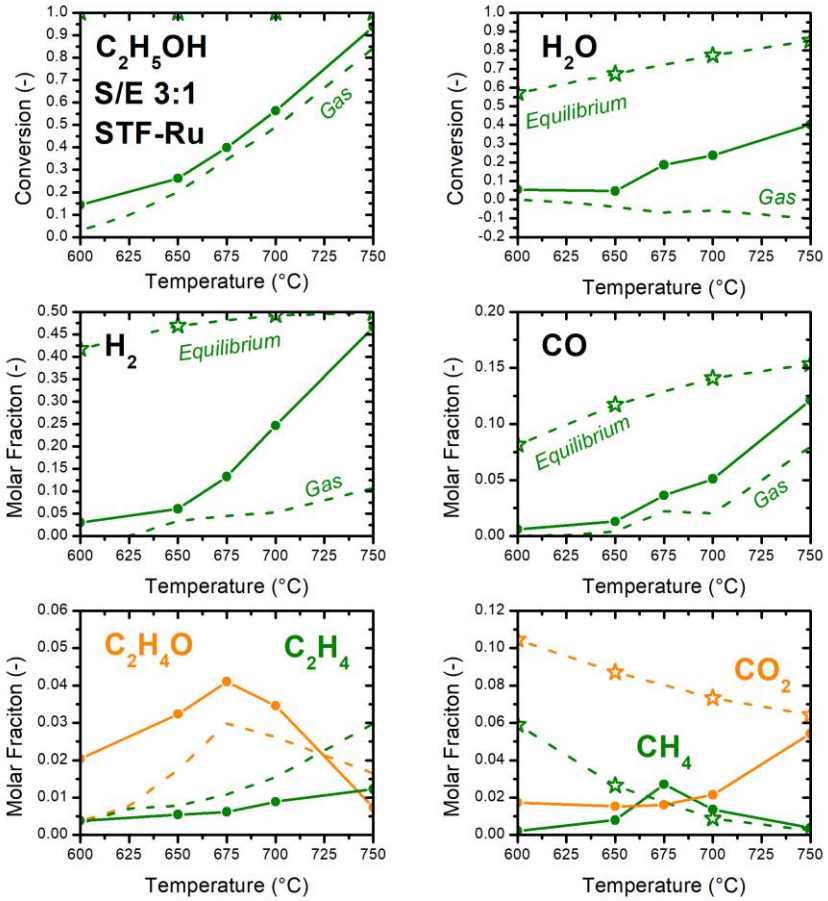
C2H5OH
S/E 3:1
STF-Ru
Gas
Conversion (-)
Temperature (°C)
H2O
Equilibrium
Gas
Conversion (-)
Temperature (°C)
H2
Equilibrium
Gas
Molar Fraciton (-)
Temperature (°C)
CO
Equilibrium
Gas
Molar Fraciton (-)
Temperature (°C)
C2H4O
C2H4
Molar Fraciton (-)
Temperature (°C)
CO2
CH4
Molar Fraciton (-)
Temperature (°C)

Figure 3

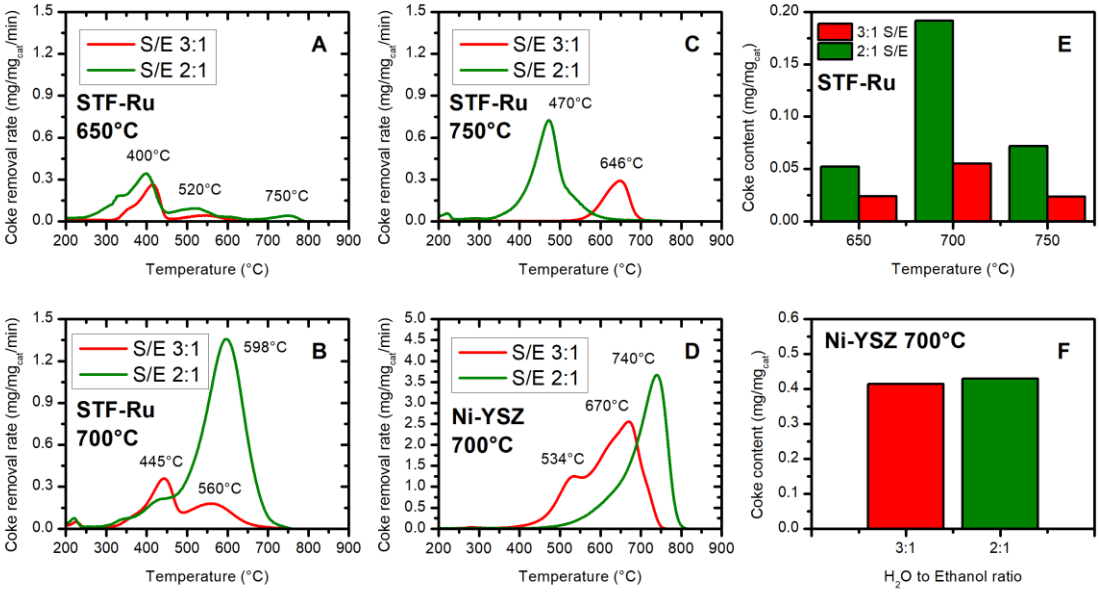

Figure 4

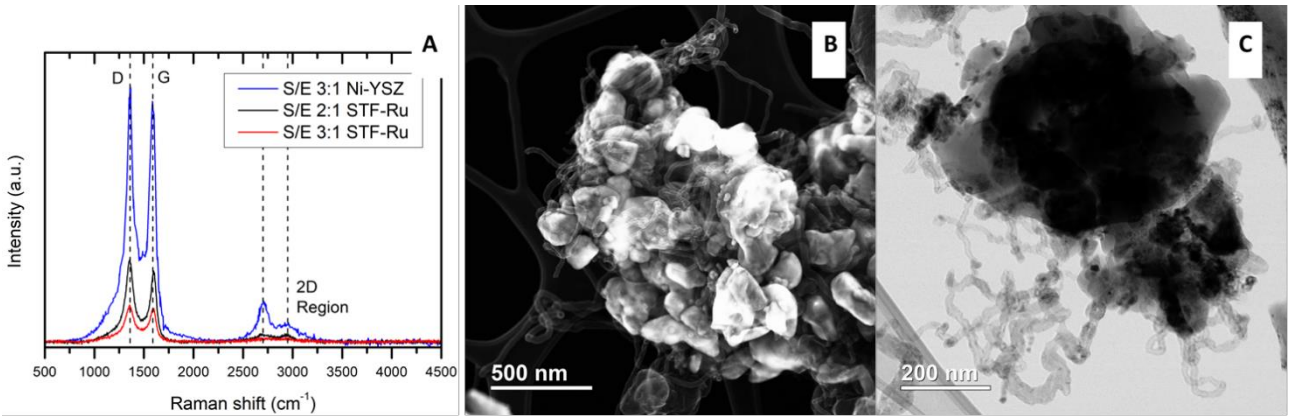

Figure 5

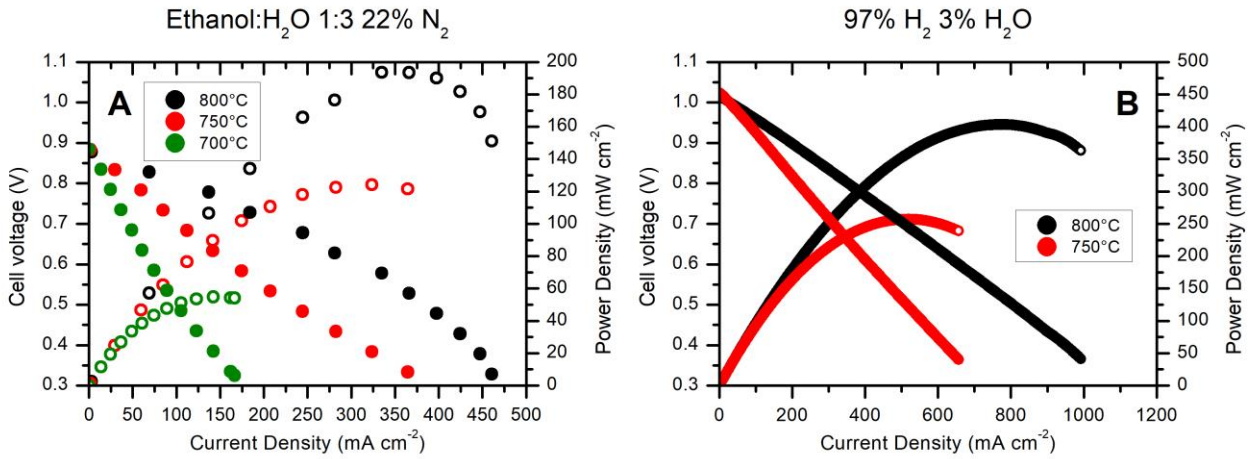
Ethanol:H2O 1:3 22% N2
A
800°C
750°C
700°C
Cell voltage (V)
Power Density (mW cm-2)
Current Density (mA cm-2)
97% H2 3% H2O
B
800°C
750°C
Cell voltage (V)
Power Density (mW cm-2)
Current Density (mA cm-2)

Figure 6

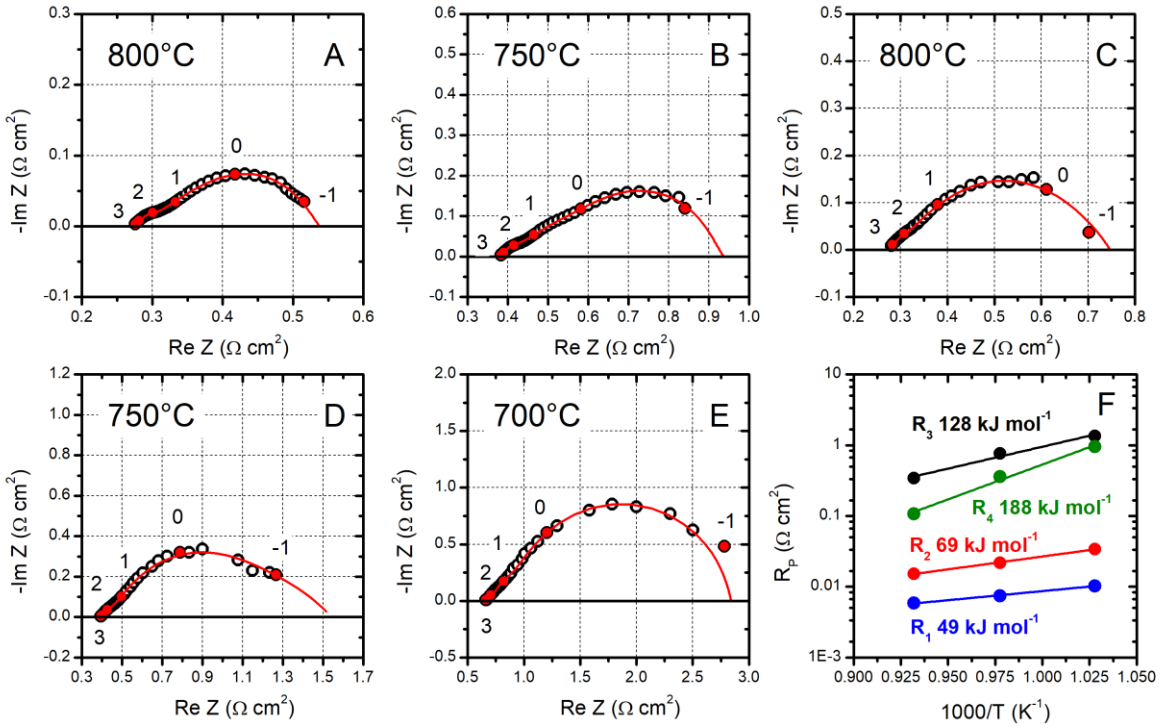
800°C
A
750°C
B
800°C
C
750°C
D
700°C
E
F
-Im Z (Ω cm²)
Re Z (Ω cm²)
R_P (Ω cm²)
1000/T (K⁻¹)
R3 128 kJ mol-1
R4 188 kJ mol-1
R2 69 kJ mol-1
R1 49 kJ mol-1

Figure 7

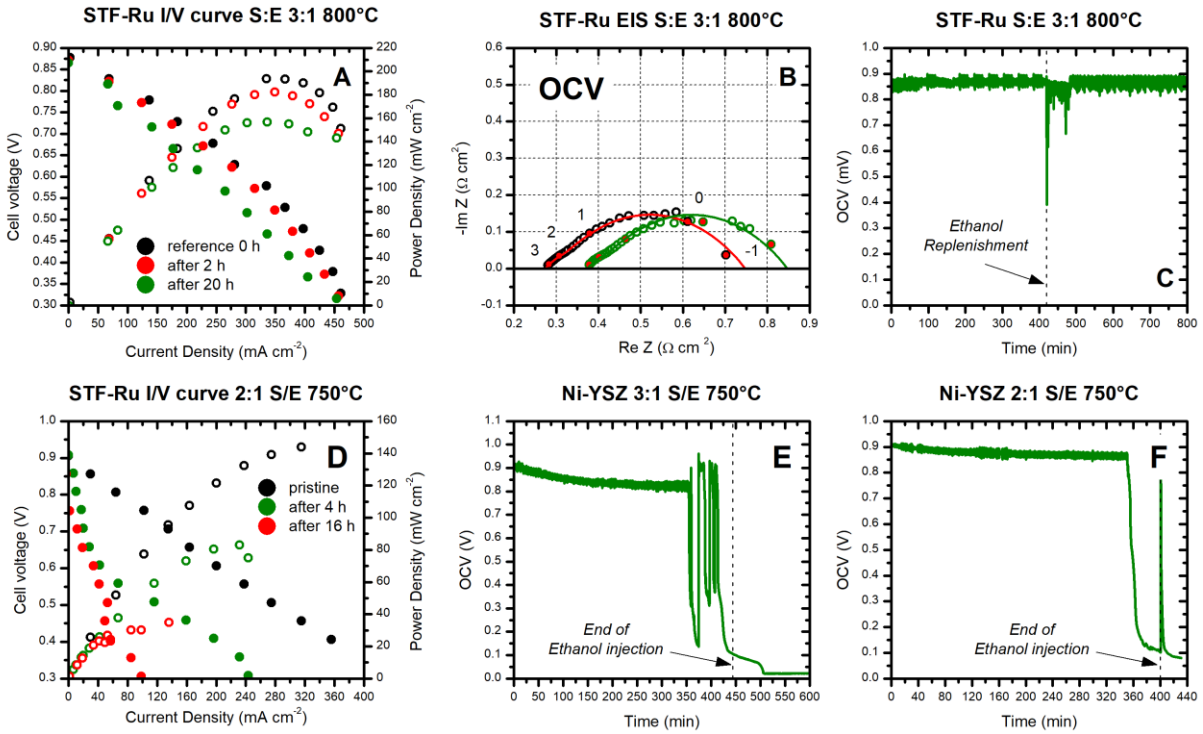
STF-Ru I/V curve S:E 3:1 800°C
A
reference 0 h
after 2 h
after 20 h
Cell voltage (V)
Power Density (mW cm-2)
Current Density (mA cm-2)
STF-Ru EIS S:E 3:1 800°C
OCV
B
-Im Z (Ω cm2)
Re Z (Ω cm 2)
STF-Ru S:E 3:1 800°C
Ethanol
Replenishment
C
OCV (mV)
Time (min)
STF-Ru I/V curve 2:1 S/E 750°C
D
pristine
after 4 h
after 16 h
Cell voltage (V)
Power Density (mW cm-2)
Current Density (mA cm-2)
Ni-YSZ 3:1 S/E 750°C
E
End of
Ethanol injection
OCV (V)
Time (min)
Ni-YSZ 2:1 S/E 750°C
F
End of
Ethanol injection
OCV (V)
Time (min)

Figure 8

Figure captions

Figure 1 – Reactants conversion and distribution of the products during the homogenous reaction of ethanol steam reforming performed in a blank quartz reactor filled with 110 mg α-Al_2O_3. The 3:1 S/E condition refers to a steam/ethanol mixture with 50 sccm flow rate and with the following molar composition: 19.5% ethanol, 58.5% H_2O, 22% N_2. The 2:1 S/E condition refers to a steam/ethanol mixture with 50 sccm and with the following molar composition: 26% ethanol, 78% H_2O, 22% N_2.

Figure 2 – Temporal evolution of ethanol conversion and inlet reactor pressure during catalytic steam reforming experiments. A) Experiments performed on STF-Ru powders at 700°C (●), 650°C (■) and 600°C (▲) with the 3:1 S/E mixture. B) Experiments performed on STF-Ru powders at 700°C (●), and 675°C (■) with the 2:1 S/E mixture. The experiments are repeated at 700°C also on STF powders (Δ). C) Experiments performed on Ni-YSZ cermet powders at 700°C (●) and 600°C (■) with the 3:1 S/E mixture. The dashed lines refer to the conversion of ethanol measured in the blank reactor, under the same conditions as in Figure 1. The catalytic powders are diluted at 1:10 ratio with α-Al_2O_3. D) Reactor pressure measured during experiments with the 3:1 S/E mixture.

Figure 3 – Steady state distribution of the products of ethanol steam reforming experiments performed on the STF-Ru catalyst with the 3:1 S/E mixture. The dashed lines refer to the molar fraction of the products measured in the gas phase experiments. The dashed lines with the star refer to the thermodynamic equilibrium composition.

Figure 4 – Results of the thermogravimetric analyses performed on STF-Ru and Ni-YSZ powders after exposure to different reaction conditions. Panels A to D show the carbon removal rate as a function of temperature, panels C and D the integral amount of carbon burned per mg of catalyst. In the case of Ni-YSZ, 17% weight gain due to the reoxidation of Ni to NiO is accounted for in the calculations (details in the Supplementary Information document).

Figure 5 – A) Raman spectra collected on STF-Ru and Ni-YSZ powders after testing at 700°C. B) TEM picture of a Ni-YSZ sample after exposure to 700°C and 2:1 S/E mixture. C) TEM picture of a STF-Ru sample after exposure to 700°C and 2:1 S/E mixture.

Figure 6 – I/V curves of STF-Ru based SOFCs measured at different temperatures and feed supply. A) 3:1 S/E mixture supply at 50 sccm flowrate. B) 3% humidified hydrogen supply with 35 sccm flow rate. Air flow rate is 135 sccm.

Figure 7 – EIS experiments measured on STF-Ru based SOFCs at OCV. The experiments with 3% humidified hydrogen supply (35 sccm) are performed at (A) 800°C, and (B) 750°C. The

experiments with 3:1 S/E mixture (50 sccm) are performed at (C) 800°C, (D) 750°C, and (E) 700°C. Operating conditions: 10 kHz − 0.1 Hz frequency range, 10 mV amplitude. The logarithm of the frequency decade is indicated. Lines are fittings with the equivalent circuit model of Figure S9. Panel F displays the Arrhenius plot of resistances R_1 to R_4 of the equivalent circuit applied to model the experiments with the S/E mixture.

Figure 8 – Effect of time on stream on I/V curves (A), impedance spectra (B), and OCV (C) measured on STF-Ru based SOFCs supplied with the 3:1 S/E mixture at 800°C. Effect of time on stream on the I/V curves of STF-Ru based SOFCs supplied at 750°C with the 2:1 S/E mixture (D); on the OCV collected at 750°C on Ni-YSZ based SOFCs supplied with the 3:1 S/E mixture (E) and with the 2:1 S/E mixture (F).

References

[1] J. Davis Steven, S. Lewis Nathan, M. Shaner, S. Aggarwal, D. Arent, L. Azevedo Inês, M. Benson Sally, T. Bradley, J. Brouwer, Y.M. Chiang, T.M. Clack Christopher, A. Cohen, S. Doig., J. Edmonds, P. Fennell, B. Field Christopher, B. Hannegan, B.M. Hodge, I. Hoffert Martin, E. Ingersoll, P. Jaramillo, S. Lackner Klaus, J. Mach Katharine, M. Mastrandrea, J. Ogden, F. Peterson Per, L. Sanchez Daniel, D. Sperling, J. Stagner, E. Trancik Jessika, K. Yang, C.J.Caldeira, Net-zero emissions energy systems, Science, 360 (2018) eaas9793.

[2] I.E.A., Global Energy Review: CO2 Emissions in 2021, (2022). https://www.iea.org/reports/global-energy-review-co2-emissions-in-2021-2.

[3] J. Goldemberg, Ethanol for a Sustainable Energy Future, Science, 315 (2007) 808–810.

[4] D. Tilman, R. Socolow, A. Foley Jonathan, J. Hill, E. Larson, L. Lynd, S. Pacala, J. Reilly, T. Searchinger, C. Somerville, R. Williams, Beneficial Biofuels—The Food, Energy, and Environment Trilemma, Science, 325 (2009) 270–271.

[5] M. Fajardy, N. Mac Dowell, Can BECCS deliver sustainable and resource efficient negative emissions?, Energy & Environmental Science, 10 (2017) 1389–1426.

[6] A.M. Hussain, E.D. Wachsman, Liquids-to-Power Using Low-Temperature Solid Oxide Fuel Cells, Energy Technology, 7 (2019) 20–32.

[7] E.D. Wachsman, C.A. Marlowe, K.T. Lee, Role of solid oxide fuel cells in a balanced energy strategy, Energy & Environmental Science, 5 (2012) 5498–5509.

[8] T.A. Schmauss, S.A. Barnett, Viability of Vehicles Utilizing On-Board CO2 Capture, ACS Energy Letters, 6 (2021) 3180–3184.

[9] Y. Jiang, A. V Virkar, A High Performance, Anode-Supported Solid Oxide Fuel Cell Operating on Direct Alcohol, Journal of The Electrochemical Society, 148 (2001) A706.

[10] K. Sasaki, K. Watanabe, Y. Teraoka, Direct-Alcohol SOFCs: Current-Voltage Characteristics and Fuel Gas Compositions, Journal of The Electrochemical Society, 151 (2004) A965.

[11] M. Lo Faro, R.M. Reis, G.G.A. Saglietti, V.L. Oliveira, S.C. Zignani, S. Trocino, S. Maisano, E.A. Ticianelli, N. Hodnik, F. Ruiz-Zepeda, A.S. Aricò, Solid oxide fuel cells fed with dry ethanol: The effect of a perovskite protective anodic layer containing dispersed Ni-alloy @ FeOx core-shell nanoparticles, Applied Catalysis B: Environmental, 220 (2018) 98–110.

[12] A.A.A. da Silva, M.C. Steil, F.N. Tabuti, R.C. Rabelo-Neto, F.B. Noronha, L. V Mattos, F.C. Fonseca, The role of the ceria dopant on Ni / doped-ceria anodic layer cermets for direct ethanol solid oxide fuel cell, International Journal of Hydrogen Energy, 46 (2021) 4309–4328.

[13] S.D. Nobrega, M. V Galesco, K. Girona, D.Z. de Florio, M.C. Steil, S. Georges, F.C. Fonseca, Direct ethanol solid oxide fuel cell operating in gradual internal reforming, Journal of Power Sources, 213 (2012) 156–159.

[14] S.D. Nobrega, P. Gelin, S. Georges, M.C. Steil, B.L. Augusto, F.B. Noronha, F.C. Fonseca, A Fuel-Flexible Solid Oxide Fuel Cell Operating in Gradual Internal Reforming, Journal of The Electrochemical Society, 161 (2014) F354–F359.

[15] M.C. Steil, S.D. Nobrega, S. Georges, P. Gelin, S. Uhlenbruck, F.C. Fonseca, Durable direct ethanol anode-supported solid oxide fuel cell, Applied Energy, 199 (2017) 180–186.

[16] E. Dogdibegovic, Y. Fukuyama, M.C. Tucker, Ethanol internal reforming in solid oxide fuel cells: A path toward high performance metal-supported cells for vehicular applications, Journal of Power Sources, 449 (2020) 227598.

[17] E. Dogdibegovic, R. Wang, G.Y. Lau, M.C. Tucker, High performance metal-supported solid oxide fuel cells with infiltrated electrodes, Journal of Power Sources, 410–411 (2019) 91–98.

[18] I.S. Pieta, A. Donazzi, C. Resini, Fuel Processing for Solid Oxide Fuel Cells BT - Modeling,

Design, Construction, and Operation of Power Generators with Solid Oxide Fuel Cells: From Single Cell to Complete Power System, in: J. Kupecki (Ed.), Springer International Publishing, Cham, 2018: pp. 97–141.

[19] W. Wang, J. Qu, P.S.B. Julião, Z. Shao, Recent Advances in the Development of Anode Materials for Solid Oxide Fuel Cells Utilizing Liquid Oxygenated Hydrocarbon Fuels: A Mini Review, Energy Technology, 7 (2019) 33–44.

[20] M. Cimenti, J.M. Hill, Direct Utilization of Liquid Fuels in SOFC for Portable Applications: Challenges for the Selection of Alternative Anodes, Energies , 2 (2009).

[21] W. Wang, Y. Chen, F. Wang, M.O. Tade, Z. Shao, Enhanced electrochemical performance, water storage capability and coking resistance of a Ni+BaZr0.1Ce0.7Y0.1Yb0.1O3−δ anode for solid oxide fuel cells operating on ethanol, Chemical Engineering Science, 126 (2015) 22–31.

[22] M.A. Azimova, S. McIntosh, On the Choice of Anode Electrocatalyst for Alcohol Fuelled Proton Conducting Solid Oxide Fuel Cells, Journal of The Electrochemical Society, 158 (2011) B1532.

[23] L. V Mattos, G. Jacobs, B.H. Davis, F.B. Noronha, Production of Hydrogen from Ethanol: Review of Reaction Mechanism and Catalyst Deactivation, Chemical Reviews, 112 (2012) 4094–4123.

[24] S. McIntosh, R.J. Gorte, Direct Hydrocarbon Solid Oxide Fuel Cells, Chemical Reviews, 104 (2004) 4845–4866.

[25] M. Rahmanipour, Y. Cheng, T.M. Onn, A. Donazzi, J.M. Vohs, R.J. Gorte, Modification of LSF-YSZ Composite Cathodes by Atomic Layer Deposition, Journal of The Electrochemical Society, 164 (2017) F879–F884.

[26] T.A. Schmauss, J.G. Railsback, M.Y. Lu, K.Y. Zhao, S.A. Barnett, ZrO2 atomic layer deposition into Sr0.5Sm0.5CoO3−δ–Ce0.9Gd0.1O2−δ solid oxide fuel cell cathodes: mechanisms of stability enhancement, Journal of Materials Chemistry A, 7 (2019) 27585–27593.

[27] T. Cao, O. Kwon, R.J. Gorte, J.M. Vohs, Metal Exsolution to Enhance the Catalytic Activity of Electrodes in Solid Oxide Fuel Cells, Nanomaterials , 10 (2020).

[28] D. Neagu, G. Tsekouras, D.N. Miller, H. Ménard, J.T.S. Irvine, In situ growth of

nanoparticles through control of non-stoichiometry, Nature Chemistry, 5 (2013) 916–923.

[29] Q. Yang, G. Liu, Y. Liu, Perovskite-Type Oxides as the Catalyst Precursors for Preparing Supported Metallic Nanocatalysts: A Review, Industrial & Engineering Chemistry Research, 57 (2018) 1–17.

[30] N. Sun, F. Jin, X. Liu, X. Liu, J. Li, Y. Shen, F. Wang, X. Chu, Z. Wu, J. Li, X. Lv, In Situ Coexsolution of Metal Nanoparticle-Decorated Double Perovskites As Anode Materials for Solid Oxide Fuel Cells, ACS Applied Energy Materials, 4 (2021) 7992–8002.

[31] Y. Wan, Y. Xing, Y. Xie, N. Shi, J. Xu, C. Xia, Vanadium-Doped Strontium Molybdate with Exsolved Ni Nanoparticles as Anode Material for Solid Oxide Fuel Cells, ACS Applied Materials & Interfaces, 11 (2019) 42271–42279.

[32] M. Cimenti, M.A. Buccheri, J.M. Hill, Direct Utilization of Methanol and Ethanol on La0.75Sr0.25Cr0.5Mn0.5O3−δ Anodes for Solid Oxide Fuel Cells, Electrocatalysis, 3 (2012) 59–67.

[33] B. Huang, S.R. Wang, R.Z. Liu, X.F. Ye, H.W. Nie, X.F. Sun, T.L. Wen, Performance of La0.75Sr0.25Cr0.5Mn0.5O3−δ perovskite-structure anode material at lanthanum gallate electrolyte for IT-SOFC running on ethanol fuel, Journal of Power Sources, 167 (2007) 39–46.

[34] N.K. Monteiro, F.B. Noronha, L.O.O. da Costa, M. Linardi, F.C. Fonseca, A direct ethanol anode for solid oxide fuel cell based on a chromite-manganite with catalytic ruthenium nanoparticles, International Journal of Hydrogen Energy, 37 (2012) 9816–9829.

[35] R. Glaser, T. Zhu, H. Troiani, A. Caneiro, L. Mogni, S. Barnett, The enhanced electrochemical response of Sr(Ti0.3Fe0.7Ru0.07)O3−δ anodes due to exsolved Ru–Fe nanoparticles, Journal of Materials Chemistry A, 6 (2018) 5193–5201.

[36] P.I. Cowin, R. Lan, C.T.G. Petit, S. Tao, Conductivity and redox stability of perovskite oxide SrFe1-xTixO3-δ ($x \leq 0.3$), Solid State Sciences, 46 (2015) 62–70.

[37] T. Zhu, H.E. Troiani, L. V. Mogni, M. Han, S.A. Barnett, Ni-Substituted Sr(Ti,Fe)O3 SOFC Anodes: Achieving High Performance via Metal Alloy Nanoparticle Exsolution, Joule, 2 (2018) 478–496.

[38] J.W.C. Liberatori, R.U. Ribeiro, D. Zanchet, F.B. Noronha, J.M.C. Bueno, Steam reforming of ethanol on supported nickel catalysts, Applied Catalysis A: General, 327 (2007) 197–204.

[39] A.N. Fatsikostas, X.E. Verykios, Reaction network of steam reforming of ethanol over Ni-based catalysts, Journal of Catalysis, 225 (2004) 439–452.

[40] D.K. Liguras, D.I. Kondarides, X.E. Verykios, Production of hydrogen for fuel cells by steam reforming of ethanol over supported noble metal catalysts, Applied Catalysis B: Environmental, 43 (2003) 345–354.

[41] G. Rabenstein, V. Hacker, Hydrogen for fuel cells from ethanol by steam-reforming, partial-oxidation and combined auto-thermal reforming: A thermodynamic analysis, Journal of Power Sources, 185 (2008) 1293–1304.

[42] D. Zanchet, J.B.O. Santos, S. Damyanova, J.M.R. Gallo, J.M.C. Bueno, Toward Understanding Metal-Catalyzed Ethanol Reforming, ACS Catalysis, 5 (2015) 3841–3863.

[43] N. Li, N. Duan, B. Liu, Q. Li, L. Jia, D. Yan, J. Li, Catalyst with CeO2 and Ni Nanoparticles on a LaCrO3-Based Perovskite Substrate for Bio-Alcohol Steam Reforming and SOFC Power Generation, ACS Applied Energy Materials, 4 (2021) 12570–12580.

[44] M. Wang, J. Yang, B. Chi, J. Pu, J. Li, High performance Ni exsolved and Cu added La0.8Ce0.2Mn0.6Ni0.4O3-based perovskites for ethanol steam reforming, International Journal of Hydrogen Energy, 45 (2020) 16458–16468.

[45] N. Li, J. Luo, L. Jia, J. Pu, B. Chi, J. Li, Ni-exsolved PrBaMn2-xNixO6-δ–based catalysts for high performance of ethanol steam reforming, Materials Today Energy, 18 (2020) 100512.

[46] P. Boldrin, E. Ruiz-Trejo, J. Mermelstein, J.M. Bermúdez Menéndez, T. Ramírez Reina, N.P. Brandon, Strategies for Carbon and Sulfur Tolerant Solid Oxide Fuel Cell Materials, Incorporating Lessons from Heterogeneous Catalysis, Chemical Reviews, 116 (2016) 13633–13684.

[47] C.H. Bartholomew, Mechanisms of catalyst deactivation, Applied Catalysis A: General, 212 (2001) 17–60.

[48] J. Vicente, C. Montero, J. Ereña, M.J. Azkoiti, J. Bilbao, A.G. Gayubo, Coke deactivation of Ni and Co catalysts in ethanol steam reforming at mild temperatures in a fluidized bed reactor, International Journal of Hydrogen Energy, 39 (2014) 12586–12596.

[49] A. Ochoa, B. Valle, D.E. Resasco, J. Bilbao, A.G. Gayubo, P. Castaño, Temperature Programmed Oxidation Coupled with In Situ Techniques Reveal the Nature and Location of Coke Deposited on a Ni/La2O3-αAl2O3 Catalyst in the Steam Reforming of Bio-oil,

ChemCatChem, 10 (2018) 2311–2321.

[50] A. Sadezky, H. Muckenhuber, H. Grothe, R. Niessner, U. Pöschl, Raman microspectroscopy of soot and related carbonaceous materials: Spectral analysis and structural information, Carbon, 43 (2005) 1731–1742.

[51] S.-L. Zhang, H. Wang, T. Yang, M.Y. Lu, C.-X. Li, C.-J. Li, S.A. Barnett, Advanced oxygen-electrode-supported solid oxide electrochemical cells with Sr(Ti,Fe)O3−δ-based fuel electrodes for electricity generation and hydrogen production, Journal of Materials Chemistry A, 8 (2020) 25867–25879.

[52] S.-L. Zhang, D. Cox, H. Yang, B.-K. Park, C.-X. Li, C.-J. Li, S.A. Barnett, High stability SrTi1−xFexO3−δ electrodes for oxygen reduction and oxygen evolution reactions, Journal of Materials Chemistry A, 7 (2019) 21447–21458.

[53] A. Nenning, L. Volgger, E. Miller, L. V Mogni, S. Barnett, J. Fleig, The Electrochemical Properties of Sr(Ti,Fe)O3-δfor Anodes in Solid Oxide Fuel Cells, Journal of The Electrochemical Society, 164 (2017) F364–F371.

[54] W. Jung, H.L. Tuller, Impedance study of SrTi1−xFexO3−δ (x=0.05 to 0.80) mixed ionic-electronic conducting model cathode, Solid State Ionics, 180 (2009) 843–847.

[55] V.M. Janardhanan, O. Deutschmann, Modeling diffusion limitation in solid-oxide fuel cells, Electrochimica Acta, 56 (2011) 9775–9782.

[56] P. Bichon, G. Haugom, H.J. Venvik, A. Holmen, E.A. Blekkan, Steam Reforming of Ethanol Over Supported Co and Ni Catalysts, Topics in Catalysis, 49 (2008) 38–45.

[57] M. Bilal, S.D. Jackson, Steam reforming of ethanol at medium pressure over Ru/Al2O3: effect of temperature and catalyst deactivation, Catalysis Science & Technology, 2 (2012) 2043–2051.

[58] S.A. Theofanidis, V. V Galvita, H. Poelman, G.B. Marin, Enhanced Carbon-Resistant Dry Reforming Fe-Ni Catalyst: Role of Fe, ACS Catalysis, 5 (2015) 3028–3039.

[59] V.A. de la Peña O'Shea, R. Nafria, P. Ramírez de la Piscina, N. Homs, Development of robust Co-based catalysts for the selective H2-production by ethanol steam-reforming. The Fe-promoter effect, International Journal of Hydrogen Energy, 33 (2008) 3601–3606.

[60] M. Domínguez, E. Taboada, E. Molins, J. Llorca, Co-Fe-Si Aerogel Catalytic Honeycombs for Low Temperature Ethanol Steam Reforming, Catalysts , 2 (2012).

[61] L. Wang, D. Li, M. Koike, S. Koso, Y. Nakagawa, Y. Xu, K. Tomishige, Catalytic performance and characterization of Ni-Fe catalysts for the steam reforming of tar from biomass pyrolysis to synthesis gas, Applied Catalysis A: General, 392 (2011) 248–255.

[62] V. Fierro, O. Akdim, C. Mirodatos, On-board hydrogen production in a hybrid electric vehicle by bio-ethanol oxidative steam reforming over Ni and noble metal based catalysts, Green Chemistry, 5 (2003) 20–24.

[63] O. Levenspiel, Chemical reaction engineering, Wiley, New York, 1999.

[64] Z. Gao, L. V Mogni, E.C. Miller, J.G. Railsback, S.A. Barnett, A perspective on low-temperature solid oxide fuel cells, Energy & Environmental Science, 9 (2016) 1602–1644.